THEORY OF LOW-MASS STARS
AND SUBSTELLAR OBJECTS

Gilles Chabrier and Isabelle Baraffe

Centre de Recherche Astrophysique de Lyon (UMR CNRS 5574),
Ecole Normale Supérieure de Lyon, 69364 Lyon Cedex 07, France;
e-mail: chabrier@ens-lyon.fr, ibaraffe@ens-lyon.fr

■ **Abstract**   Since the discovery of the first bona-fide brown dwarfs and extra-solar planets in 1995, the field of low-mass stars and substellar objects has progressed considerably, both from theoretical and observational viewpoints. Recent developments in the physics entering the modeling of these objects have led to significant improvements in the theory and to a better understanding of these objects' mechanical and thermal properties. This theory can now be confronted with observations directly in various observational diagrams (color-color, color-magnitude, mass-magnitude, mass-spectral type), a stringent and unavoidable constraint that became possible only recently with the generation of synthetic spectra. In this paper we present the current state-of-the-art general theory of low-mass stars and sub stellar objects, from one solar mass to one Jupiter mass, regarding primarily their interior structure and evolution. This review is a natural complement to the previous review by Allard et al (1997) on the atmosphere of low-mass stars and brown dwarfs. Special attention is devoted to the comparison of the theory with various available observations. The contribution of low-mass stellar and sub stellar objects to the Galactic mass budget is also analyzed.

1.   INTRODUCTION

Interest in the physics of objects at the bottom of and below the Main Sequence (MS) originated in the early demonstration by Kumar (1963) that hydrogen-burning in a stellar core no longer occurs below a certain mass, and that below this limit hydrostatic equilibrium against gravitational collapse is provided by electron degeneracy. Simple analytical arguments, based on the balance between the classical ionic thermal pressure and the quantum electronic pressure, yielded for this H-burning minimum mass (HBMM) $m_{\mathrm{HBMM}} \approx 0.1\ M_{\odot}$, whereas the first detailed evolutionary calculations gave $m_{\mathrm{HBMM}} \approx 0.085\ M_{\odot}$ (Grossman et al 1974). Tarter

(1975) proposed the term "brown dwarfs" (BD) for objects below this H-burning limit. D'Antona & Mazzitelli (1985) first pointed out that the luminosity below m_{HBMM} would stretch by a few orders of magnitude over a few hundredths of a solar mass, making the observation of BDs a tremendously difficult task. Subsequent benchmarks in low-mass star (LMS) and BD theory came primarily from VandenBerg et al (1983), D'Antona & Mazzitelli (1985), Dorman et al (1989), Nelson et al (1986, 1993a) and the Tucson group (Lunine et al 1986, 1989; Burrows et al 1989, 1993). In spite of this substantial theoretical progress, all of these models failed to reproduce the observations at the bottom of the MS and thus could not provide a reliable determination of the characteristic properties (mass, age, effective temperature, luminosity) of low-mass stellar and substellar objects. A noticeable breakthrough came from the first calculations by a few groups of synthetic spectra and atmosphere models characteristic of cool ($T_{eff} \lesssim 4000$ K) objects (Allard 1990, Brett & Plez 1993, Saumon et al 1994, Allard & Hauschildt 1995, Brett 1995, Tsuji et al 1996, Hauschildt et al 1999). This allowed the computation of consistent non-grey evolutionary models (Saumon et al 1994, Baraffe et al 1995) and the direct confrontation of theory and observation in photometric passbands and color-magnitude diagrams, thus avoiding dubious transformations of observations into theoretical L-T_{eff} Hertzsprung-Russell diagrams.

In the meantime, the search for faint (sub)stellar objects has bloomed over the past few years. Several BDs have now been identified since the first discoveries of bona-fide BDs (Rebolo et al 1995, Oppenheimer et al 1995), either in young clusters (see Basri, this volume, and Martín 1999 for reviews and references therein) or in the Galactic field (Ruiz et al 1997, Delfosse et al 1997, Kirkpatrick et al 1999a). The steadily increasing number of identified extra-solar giant planets (EGPs) since the discovery of 51PegB (Mayor & Queloz 1995; see Marcy & Butler 1998 for a review) has opened up a new era in astronomy. Ongoing and future ground-based and space-based optical and infrared surveys of unprecedented faintness and precision are likely to reveal several hundred more red dwarfs, brown dwarfs, and giant planets, which will necessitate the best possible theoretical foundation. The correct understanding of the physical properties of these objects bears major consequences for a wide range of domains of physics and astrophysics—namely, dense matter physics, planet and star formation and evolution, galactic evolution, and missing mass.

A general outline of the basic physics entering the structure and the evolution of BDs can be found in the excellent reviews of Stevenson (1991) and Burrows & Liebert (1993). It is the aim of this review to summarize the most recent progress realized in the theory of LMS, BDs, and EGPs. We focus mainly on the internal structure and the evolution of these objects, since a comprehensive review on the atmosphere of LMS and BDs appeared recently (Allard et al 1997). We also consider the implications of LMS and BDs in a more general galactic context and evaluate their contribution to the Galactic mass budget.

2.   THE PHYSICS OF DENSE OBJECTS

2.1   Interior Physics

2.1.1 Equation of State   Central conditions for LMS—hereafter identified generically as objects below a solar mass—and for substellar objects (SSO) for solar composition range from a maximum density $\rho_c \simeq 10^3$ gcm^{-3} at the hydrogen-burning limit ($m \approx 0.07\,M_\odot$, see below) to $\rho_c \simeq 10$ gcm^{-3} for Saturn ($= 5 \times 10^{-4}$ $M_\odot$) at 5 Gyr, and from $T_c \simeq 10^7$ K for the Sun to $T_c \simeq 10^4$ K for Saturn at the same age, spanning several orders of magnitudes in mass, density, and temperature. Effective temperatures range from $\sim$6000 K to $\sim$2000 K in the stellar domain and extend down to $\sim$100 K for Saturn. Molecular hydrogen and other molecules become stable for $kT \lesssim 3 \times 10^{-2}$ Ryd ($T \approx 5 \times 10^3$ K), a condition encountered in the atmosphere, or even deeper layers, of most of these objects. Under these conditions, the interior of LMS and SSO is essentially a fully ionized H$^+$/He^{++} plasma characterized by coupling parameters $\Gamma_i = \langle Z^{5/3}\rangle e^2/a_e kT \approx 0.1-50$ for classical ions and $r_S = \langle Z\rangle^{-1/3}a/a_0 \approx 0.1-1$ for degenerate electrons. With $\Gamma_i = \langle Z^{5/3}\rangle(2.693 \times 10^5 \text{ K}/T)n_{24}^{1/3}$, $r_S = 1.39/(\rho/\mu_e)^{1/3} = 1.172\,n_{24}^{-1/3}$, $n_{24} \equiv n_e/10^{24}$ cm$^{-3} \approx (\rho/1.6605 \text{ gcm}^{-3})\mu_e^{-1}$ the electron number-density, $a = (\frac{3}{4\pi}\frac{V}{N_i})^{1/3} = a_e\langle Z\rangle^{1/3}$ is the mean interionic distance, $\mu_e^{-1} = \langle Z\rangle/\langle A\rangle$ is the electron mean molecular weight, ρ is the mass-density, A is the atomic mass, a_0 is the electronic Bohr radius, and $\langle\rangle$ denotes the average number-fraction $\langle X\rangle = \sum_i x_i X_i$ ($x_i = N_i/\sum_i N_i$). The temperature is of the order of the electron Fermi temperature T_F so that the degeneracy parameter $\psi = kT/kT_F \approx 3.314 \times 10^{-6}\,T\,(\mu_e/\rho)^{2/3}$ is of the order of unity. The classical (Maxwell-Boltzman) limit corresponds to $\psi \to +\infty$, whereas $\psi \to 0$ corresponds to complete degeneracy. The aforementioned thermodynamic conditions yield $\psi \approx 2$–0.05 in the interior of LMS and BDs, which implies that finite-temperature effects for the electrons must be included to accurately describe the thermodynamic properties of the correlated, partially degenerate electron gas. Moreover, the Thomas-Fermi wavelength $\lambda_{TF} = \left(kT_F/(6\pi n_e e^2)\right)^{1/2}$ is of the order of a, so that the electron gas is polarized by the external ionic field, and electron-ion coupling must be taken into account in the plasma hamiltonian. Last but not least, the electron average binding energy can be of the order of the Fermi energy $Ze^2/a_0 \sim \epsilon_F$ so that *pressure*-ionization takes place along the internal profile. Figure 1 illustrates central characteristic quantities for LMS and SSOs from the Sun to Jupiter.

Above $\sim 0.4\,M_\odot$, the structure evolves slowly with increasing mass from a $n = 3/2$ towards a $n = 3$ polytrope, which yields the correct P_c for the Sun, as a result of the growing central radiative core. This leads to increasing central pressures and densities for increasing mass (increasing polytropic index) in this mass range. Below $\sim$0.3–0.4 $M_\odot$, the core becomes entirely convective and follows the behavior of a $n = 3/2$ polytrope. Because the gas is still in the classical regime ($\psi \gtrsim 1$), $m \propto R$ and the central density increases with decreasing mass,
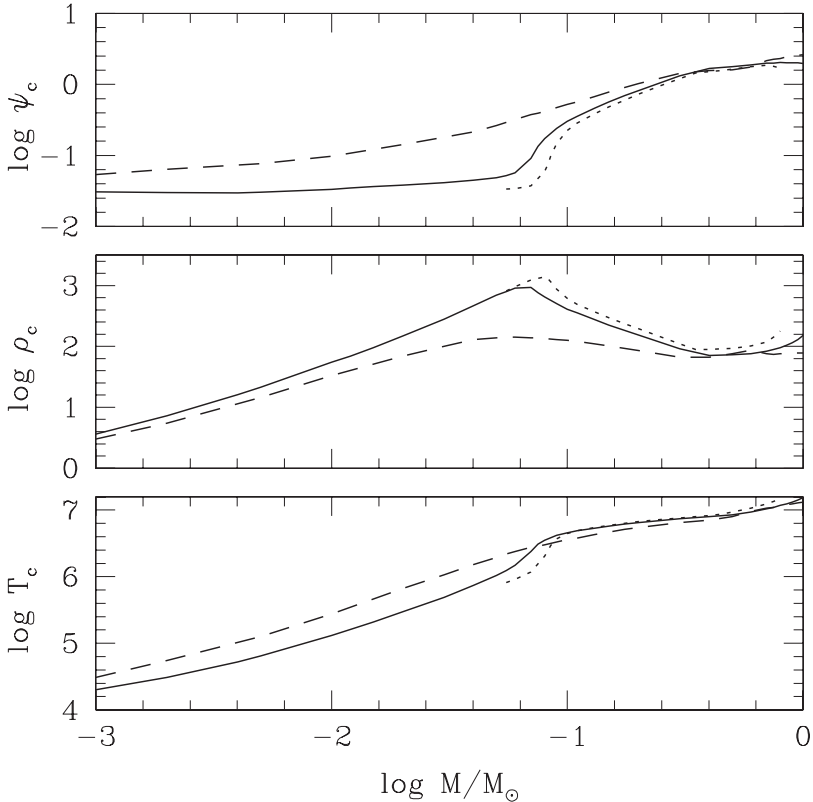
Figure 1   Central temperature (in K), density (in g cm^{-3}), and degeneracy parameter along the LMS-SSO mass range for objects with $Z = Z_\odot$ at 5 Gyr (*solid line*) and 10^8 yr (*dashed line*), and with a metallicity $Z = 10^{-2} Z_\odot$ at 5 Gyr (*dotted-line*).

$\rho_c \propto m^{-2}$. Below the H-burning limit, electron degeneracy becomes dominant ($\psi \lesssim 0.1$), so that one approaches the relation $m \propto R^{-3}$ (for $\psi = 0$), and density decreases again with decreasing mass, $\rho_c \propto m^2$. These various effects yield a non-monotomic behavior of the central density and pressure with mass, with a minimum in the stellar regime around $0.4\ M_\odot$ and a maximum near the H-burning limit.

The equation of state (EOS) of low-mass objects thus requires a detailed description of strongly correlated, polarizable, partially degenerate classical and quantum plasmas, plus an accurate treatment of pressure partial ionization, a severe challenge for dense matter physicists. Several steps toward the derivation of such an accurate EOS for dense astrophysical objects have been realized since the pioneering work of Salpeter (1961), with major contributions by Fontaine et al (1977), Magni & Mazzitelli (1979), Marley & Hubbard (1988) (for objects

with $m < 0.2\ M_\odot$), Hümmer & Mihalas (1988) (primarily devoted to conditions characteristic of solar-type stellar envelopes), and Saumon & Chabrier (Chabrier 1990; Saumon & Chabrier 1991, 1992; Saumon et al 1995; hereafter SCVH). We refer the reader to Saumon (1994) and SCVH for a detailed review and an extensive comparison of these different EOSs in the domain of interest. The SCVH EOS presents a consistent treatment of pressure ionization and includes significant improvements with respect to previous calculations in the treatment of the correlations in dense plasmas. It compares well with available high-pressure shock-wave experiments in the molecular domain, and with Monte-Carlo simulations in the fully-ionized, metallic domain (see references above for details). Recently, laser-driven shock-wave experiments on D_2 have been conducted at Livermore (Da Silva et al 1997, Collins et al 1998); these experiments were the first to reach the pressure-dissociation and ionization domain and thus directly probe the thermodynamic properties of dense hydrogen under conditions characteristic of BDs and giant planets (GP). The relevance of these experiments for the interior of SSOs can be grasped from Figure 1 of Collins et al (1998). These experiments have shown good agreement between the predictions of the Saumon-Chabrier model and the actual data (although there is certainly room for improvement). In particular, the strong compression factor arising from hydrogen pressure-dissociation and ionization observed in the experiment ($\rho/\rho_i \sim 5.8$) agrees well with the predicted theoretical value (see Figure 3 of Collins et al 1998). Any EOS devoted to the description of the interior of dense astrophysical objects must now be confronted with these available data.

The SCVH EOS is a pure hydrogen and helium EOS, based on the so-called additive-volume law between the pure components (H and He). The accuracy of the additive-volume-law has been examined in detail by Fontaine et al (1977). The invalidity of this approximation for accurately describing the thermodynamic properties of the mixture is significant only in the *partial ionization* region (see SCVH), which concerns only a few percent of the stellar mass under LMS and BD conditions. The effect of metals on the structure and the evolution of these objects has been examined in detail by Chabrier & Baraffe (1997; Section 2.1). These authors show that because of their negligible number-abundance ($\sim 0.2\%$), metals do not contribute significantly to the EOS and barely modify the structure and evolution ($\sim 1\%$ in $T_{\rm eff}$ and $\sim 4\%$ in L) of these objects. In the low-density limit characteristic of the atmosphere, the SCVH EOS recovers the perfect gas limit, and thermal contributions from various atomic or molecular species can be added within the aforementioned additive-volume law formalism, which is exact in this regime. Only in the (denser) metal-depleted atmospheres ($Z \lesssim 10^{-2}\ Z_\odot$) of the densest objects ($\lesssim 0.1\ M_\odot$) does one find a slight departure from ideality, with a 1% to 4% effect on the adiabatic gradient ∇_{ad} (Chabrier & Baraffe 1997).

2.1.2 Nuclear Rates. Screening Factors Although the complete PP chain is important for nucleosynthesis, the thermonuclear processes relevant from the energetic viewpoint under LMS and BD conditions are given by the PPI chain (see

e.g. Burrows & Liebert 1993, Chabrier & Baraffe 1997):

$$p + p \rightarrow d + e^+ + \nu_e; \quad p + d \rightarrow {}^3He + \gamma; \quad {}^3He + {}^3He \rightarrow {}^4He + 2p. \quad (1)$$
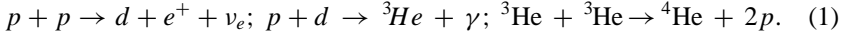
Below $\sim 0.7\, M_\odot$, the PPI chain contributes to more than 99% of the energy generation on the zero-age Main Sequence (ZAMS), and the PPII chain to less than 1%. The destruction of ${}^3He$ by the above reaction is important only for $T > 6 \times 10^6$ K, i.e masses $m \gtrsim 0.15\, M_\odot$ for ages $t < 10$ Gyr, for which the lifetime of this isotope against destruction becomes eventually smaller than a few Gyr.

As examined in Section 4.6, the abundance of light elements (*D*, *Li*, *Be*, *B*) provides a powerful diagnostic for identifying the age and/or mass of SSOs. The rates for these reactions (see e.g. Nelson et al 1993b) in the vacuum, or in an almost perfect gas where kinetic energy largely dominates the interaction energy, are given by Caughlan & Fowler (1988) and Ushomirsky et al (1998) for updated values. The reaction rate R_0 (in $\text{cm}^{-3}s^{-1}$) in the vacuum is given by $R_0 \propto e^{-3\epsilon_0/kT}$, where ϵ_0 corresponds to the Gamow-peak energy for non-resonant reactions (Clayton 1968). However, as we mentioned in the previous section, non-ideal effects dominate in the interior of LMS and BDs and lead to polarization of the ionic and electronic fluids. These polarization effects resulting from the surrounding particles yield an enhancement of the reaction rate, as was first recognized by Schatzman (1948) and Salpeter (1954). The distribution of particles in the plasma reads:

$$n(r) = \bar{n} e^{-Ze\phi(r)/kT}, \quad \text{with} \quad \phi(r) = \frac{Ze}{r} + \psi(r), \quad (2)$$

where $\psi(r)$ is the induced mean field potential resulting from the polarization of the surrounding particles. This induced potential lowers the Coulomb barrier between the fusing particles and thus yields an enhanced rate in the plasma $R = E \times R_0$, where

$$E = \lim_{r \to 0} \left\{ g_{12}(r) exp \left(\frac{Z_1 Z_2 e^2}{rkT} \right) \right\} \quad (3)$$

is the enhancement (screening) factor and $g_{12}(r)$ is the pair-distribution function of particles in the plasma. Under BD conditions, ion screening must be considered as well as electron screening, i.e. $E = E_i \times E_e$. Both effects are of the same order ($E_i \sim E_e \sim$ a few) and must be included in the calculations for a correct estimate of the light element-depletion factor (see Section 4.6). Figure 2 portrays the evolution of the central temperature for objects respectively above, at the limit of, and below the hydrogen-burning minimum mass, with lines indicating the hydrogen, lithium, and deuterium burning temperatures in the plasma.

2.1.3 Transport Properties Energy in the interior of LMS below $\sim 0.4\, M_\odot$, BDs, and GPs is transported essentially by convection (see e.g. Stevenson 1991). According to the mixing length theory (MLT), the convective flux reads (Cox
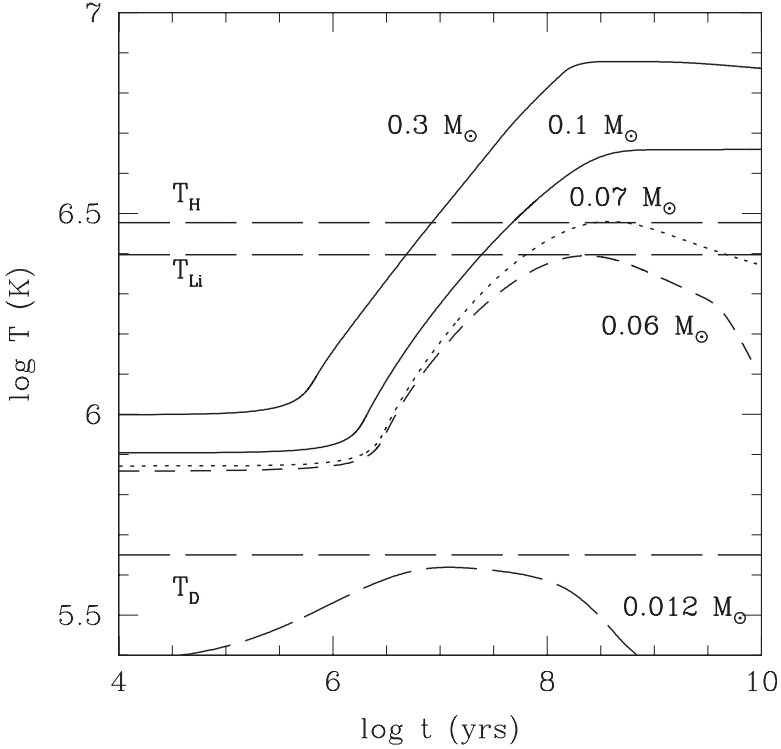
Figure 2 Central temperature as a function of age for different masses. T_H, T_{Li}, and T_D indicate the hydrogen, lithium, and deuterium burning temperatures, respectively.

& Giuli 1968):

$$F_{conv} \propto \rho v_{conv} C_P \delta T \propto \left(Q^{1/2}/\Gamma_1^{1/2}\right)\left(\frac{l}{H_P}\right)^2 \rho C_P c_S T (\nabla - \nabla_e)^{3/2}, \quad (4)$$

where $Q = -(\frac{\partial \ln \rho}{\partial \ln T})_P$ is the volume expansion coefficient, C_P is the specific heat at constant pressure, $c_S = (\Gamma_1 P/\rho)^{1/2}$ is the adiabatic speed of sound, δT is the temperature excess between the convective eddy and the surrounding ambient medium, ∇ is the temperature gradient, v_{conv} is the convective velocity, l and H_P denote the mixing length and the pressure scale height, respectively, and $\nabla_e \sim \nabla_{ad}$ is the eddy temperature gradient. The last term in parentheses on the righthand side of Equation 4 defines the fluid superadiabaticity, i.e. the fractional amount by which the real temperature gradient exceeds the adiabatic temperature gradient. Below a certain mass, the inner radiative core vanishes and the star becomes entirely convective (VandenBerg et al 1983, D'Antona & Mazzitelli 1985, Dorman et al 1989). This minimum mass, calculated with consistent non-grey atmosphere

models and with the most recent OPAL radiative opacities (Iglesias & Rogers 1996) for the interior, is found to be $m_{conv} = 0.35\ M_\odot$ within the metallicity range $10^{-2} \leq Z/Z_\odot \leq 1$ (Chabrier & Baraffe 1997; Section 3.2). The Rayleigh number is defined as $Ra = \frac{gQH_P^3}{\xi\nu}(\nabla - \nabla_{\mathrm{ad}})$, where $g \sim 10^3-10^5$ cm s^{-2} is the surface gravity, ξ is the thermal diffusivity (conductive or radiative diffusivity), and ν is the kinematic viscosity. In the interior of LMS, $Ra \sim 10^{25}$ so that convection is almost perfectly adiabatic and the MLT provides a fairly reasonable description of this transport mechanism. Variation of the MLT parameter $\alpha = l/H_P$ between 1 and 2 in the interior is found to be inconsequential below $\sim 0.6\ M_\odot$ (see Baraffe et al 1997).

However, convection can be affected or even inhibited by various mechanisms. Maximum rotation velocities for LMS and BDs are usually in the range ~ 20–30 km s^{-1} (see e.g. Delfosse et al 1998a) with values as large as 50 km s^{-1} and 80 km s^{-1} in the extreme case of Kelu 1 (Ruiz et al 1997, Basri et al 2000). This corresponds to an angular velocity $\Omega \sim 5 \times 10^{-4}$ rad s^{-1} for a characteristic radius $R \sim 0.1\ R_\odot$ ($\Omega_{Jup} = 1.76 \times 10^{-4}$ rad s^{-1}). Within most (>95% in mass) of the interior of LMS and BDs, v_{conv} is of the order of 10^2 cm s^{-1} ($\ll c_S$) and $H_P \sim 10^9$ cm. Thus, the Rossby number $Ro = v_{conv}/\Omega l \approx 10^{-3}$, where $l \sim H_P$, and convection in principle can be inhibited by rotation. However, the fact that lithium is not observed in objects with $m \gtrsim 0.06\ M_\odot$ (see Section 4.6) suggests that some macroscopic transport mechanism (e.g. meridional circulation, turbulence, or convection) remains efficient throughout the star. The Reynolds number $Re = v_{conv}\,l/\nu$ remains largely above unity in stellar and SSO interiors, so that convection is not inhibited by viscosity. Magnetic inhibition requires a magnetic velocity $v_A = (B^2/4\pi\rho)^{1/2} > v_{conv}$ (Stevenson 1979, 1991), i.e. $B \gtrsim 10^4$ Gauss under the conditions of interest, which is only slightly above the predicted fields in these objects (see Section 2.3). However, Stevenson (1979) proposed that in a rapidly rotating fluid with a significant magnetic field, the Proudman-Taylor theorem no longer applies, so that vertical convective motions could be possible. Last, convection efficiency can be diminished by the presence of a density gradient. As shown by Guillot (1995), this may occur in the interior of gaseous planets because of a gradient of heavy elements, thus leading to inefficient convective transport in the envelope of these objects.

The treatment of convection in the outer (molecular) layers, above and near the photosphere, is a more delicate question. The Rayleigh number in this region is $Ra \sim 10^{15}$, a rather modest value by the usual standards in turbulence. Since the MLT, by definition, applies to the asymptotic regime $Ra \to \infty$, it is no longer valid near the photosphere. Much work has been devoted to the improvement of this formalism and to the derivation of a non-local treatment of convection. One of the most detailed attempts came from Canuto and Mazzitelli (Canuto & Mazzitelli 1991; CM). The original CM formalism was based on a linear stability analysis, whereas energy transport by turbulence is a strongly non-linear process. It was improved recently by the inclusion to some extent of non-linear modes in the

energy rate (Canuto et al 1996), but it yields results similar to the initial CM model. The formalism, however, still requires the calibration of a free parameter, which represents a characteristic "mixing" scale and in this sense resembles the MLT. A more severe shortcoming of the CM formalism is that the predicted outermost limit of the convection zone for the Sun and the amount of superadiabaticity in this zone disagree significantly, both quantitatively and qualitatively, with the results obtained from coupled hydrodynamic-radiation 3D simulations (Demarque et al 1999, Nordlund & Stein 1999). The 3D simulations yield excellent agreement with the observational data at several diagnostic levels: the thermal structure (and the inferred depth of the convection zone), the dynamical structure (vertical velocity amplitude and spectral line synthesis), and the p-mode frequencies and amplitudes for the Sun, without the use of free parameters (see e.g. Spruit & Nordlund 1990 for a review, also Nordlund & Stein 1999). This now provides a high degree of confidence in 3-D hydrodynamic models of stellar surface layers and the inferred transition from convective to radiative energy transport.

The thermal structure, for example, is a very robust property of the numerical models, since it depends relatively little on the level of turbulence (and thus on numerical resolution) (Stein & Nordlund 2000, Nordlund & Stein 1999). These results illustrate the fact that any formalism based on a homogeneous description of convection (e.g. MLT, CM) cannot accurately describe this strongly inhomogeneous process. Interestingly enough, the standard MLT is found to compare reasonably well with these simulations, at least for the thermal profile (see aforementioned references), and thus seems to offer a reasonable (or least worst!) overall description of convective transport, even in the small-efficiency convective regions. Indeed, in contrast to 1-D models computed with the CM formalism, the 3-D models do not have a steeper and more narrow superadiabatic structure for the Sun than was obtained with the classical Böhm-Vitense mixing length recipe (Nordlund & Stein 1999). It it thus fair to say that, in the absence of a correct non-local treatment of convection in LMS and BD interiors, the standard MLT is probably the most reasonable choice—at least for the present objects, LMS and SSOs. Clearly, the development of 3-D hydrodynamic models of the atmosphere of these objects and the calibration of the mixing length from these simulations, as is done for solar-type stars (Ludwig et al 1999), represents one of the next major challenges in the theory.

Another possible mechanism of energy transport in stellar interiors is conduction. Its efficiency can be estimated as follows: The distance l over which the temperature changes significantly is $l \sim (\chi t)^{1/2}$, where χ is the thermal diffusivity and t is the time during which the temperature change occurs. For $\chi \sim 10^{-1}$ cm^2 s^{-1}, characteristic of metals, and $t \sim 10^9$ yr, $l \sim 10^2$ km. Thus, heat can possibly be transported by conduction only over a limited range of the interior, providing that the density is high enough and the temperature low enough for electron conductivity to become important. Indeed, below the HBMM $\sim 0.07 \, M_\odot$, the interior becomes degenerate enough during cooling that the conductive flux

$F_{\rm cond} = K_{\rm cond}\nabla T$, where $K_{\rm cond} = \frac{4ac}{3}\frac{T^3}{\rho\kappa_{\rm cond}}$ and $\kappa_{\rm cond}$ is the conductive opacity, becomes larger than the convective flux. Old enough BDs in the mass-range 0.02–0.07 $M_\odot$ become degenerate enough to develop a conductive core, which slows down the cooling $L(t)$ (Chabrier et al 2000).

2.2 Atmosphere

Knowledge of the atmosphere is needed for two reasons: (1) as a boundary condition for the interior profile in the optically-thick region, and (2) as a description of the emergent radiative flux. A comprehensive review of the physics of the atmosphere of LMS and BDs can be found in Allard et al (1997). Only a general outline of the main characteristics of these atmospheres is mentioned in the present review.

2.2.1 Spectral Distribution Surface gravity $g = Gm/R^2$ for LMS and SSOs range from $\log g \simeq 4.4$ for a main sequence 1.0 $M_\odot$ star to $\log g \simeq 3.4$ for Jupiter, with a maximum $\log g \simeq 5.5$ at the H-burning limit, for solar metallicity. This yields $P_{ph} \sim g/\bar{\kappa} \sim 0.1 - 10$ bar and $\rho_{ph} \sim 10^{-6}$–10^{-4} g cm^{-3} at the photosphere. Collision effects become significant under these conditions and induce molecular dipoles on e.g. H$_2$ or He-H$_2$, yielding so-called collision-induced absorption (CIA) between roto-vibrational states of molecules that otherwise would have only quadrupolar transitions (Linsky 1969, Borysow et al 1997). At first order this CIA coefficient scales as $\kappa_{CIA} \propto n_{H_2}^2 \times \kappa_{H_2H_2}$ and thus becomes increasingly important as soon as H$_2$ molecules become stable. The CIA of H$_2$ suppresses the flux longward of 2 μm in the atmosphere of LMS, BDs, and GPs. This is one of the reasons (the main one for metal-depleted objects) for the redistribution of the emergent radiative flux toward shorter wavelengths in these objects (Lenzuni, Chernoff & Salpeter 1991, Saumon et al 1994, Allard & Hauschildt 1995, Baraffe et al 1997). The CIA of H$_2$ and H$_2$-He and the bound-free and free-free opacities of H$^-$ and H$_2^-$ provide the main continuum opacity sources below $\sim$5000 K for objects with metal-depleted abundances. Below $T_{\rm eff} \lesssim 4000$ K, most of the hydrogen is locked into H$_2$, and most of the carbon in CO. Excess oxygen is bound in molecules such as TiO, VO and H$_2$O, with some amounts also in OH and O (see e.g. Figure 1 of Fegley & Lodders 1996). Metal oxides and metal hydrides (FeH, CaH, MgH) are also present. The energy distribution of solar-abundance M-dwarfs is thus entirely governed by the line absorption of TiO and VO in the optical, and H$_2$O and CO in the infrared, with no space for a true continuum. The VO and TiO band strength indexes are used to classify M-dwarf spectral types (see e.g. Kirkpatrick et al 1991). The strongly frequency-dependent absorption coefficient resulting from line transitions of these molecules, along with Rayleigh scattering ($\propto \nu^4$) shortward of $\sim$0.4 μm, yield a strong departure from a black-body energy distribution (see e.g. Figure 5 of Allard et al 1997).

At $T_{\rm eff} \approx 2000$ K, near the H-burning limit, signatures of metal oxides and hydrides (TiO, VO, FeH, CaH bands) disappear from the spectral distribution

(although some amount of TiO remains present in the atmosphere), as observed e.g. in GD 165B (Kirkpatrick et al 1999b). Alkalies are present under their atomic form. The disappearance of TiO-bands prompted astronomers to suggest a new spectral type classification, the "L"-type, for objects with T_{eff} below the afore-mentioned limit (Martín et al 1997, 1998, Kirkpatrick et al 1999a). Below a local temperature T $\approx$ 1300–1500 K, P $\sim$ 3–10 bar for a solar abundance-distribution, carbon monoxide CO was predicted to dissociate and the dominant equilibrium form of carbon was predicted to become CH_4 (Allard & Hauschildt 1995, Tsuji et al 1995, Fegley & Lodders 1996). Note that this transition occurs gradually, with some of the two elements present in the stability field of the other (see e.g. Fegley & Lodders 1996, Lodders 1999), so that cool stars could contain some limited amount of methane, and CO may be visible in objects with $T_{eff} < 1800$ K as indeed detected in G1229B (Noll et al 1997; Oppenheimer et al 1998). This prediction has been confirmed by the spectroscopic observation of Gliese229B and the identification of methane absorption features at 1.7, 2.4, and 3.3 μm (Oppenheimer et al 1995). The presence of methane in its spectrum unambiguously confirmed its sub-stellar nature (Oppenheimer et al 1995, Allard et al 1996, Marley et al 1996). Objects like Gl229B, characterized by the strong signature of methane absorption in their spectra, define a new spectral class of objects, the "methane" (sometimes called "T") BDs. Methane absorption in the H and K bands yields a steep spectrum at shorter wavelengths and thus blue near infrared colors, with $J - K \lesssim 0$, but $I - J \gtrsim 5$ (Kirkpatrick et al 1999a, Allard 1999). Although the transition temperature between "L" and "methane" dwarfs is not precisely determined yet, it should lie in the range $1000 \lesssim T_{eff} \lesssim 1700$ K (see Section 4.5.2).

Below $T_{eff} \sim 2800$ K, complex O-rich compounds condense in the atmosphere, slightly increasing the carbon:oxygen abundance ratio (see e.g. Tsuji et al 1996, Fegley & Lodders 1996, Allard et al 1997). Different constituents will condense at a certain location in the atmosphere with an abundance determined by chemical equilibrium conditions (although non-equilibrium material may form, depending on the time-scale of the reactions, as mentioned below) between the gas phase and the condensed species. The formation of condensed species depletes the gas phase of a number of molecular species (e.g. VO, TiO, which will be sequestered into perovskite $CaTiO_3$), significantly modifying the emergent spectrum (see e.g. Fegley & Lodders 1994 for the condensation chemistry of refractory elements in Jupiter and Saturn). The equilibrium abundances can be determined from the Gibbs energies of formation either by minimization of the total Gibbs energy of the system (Sharp & Huebner 1990, Burrows & Sharp 1999), or by computing the equilibrium pressures of each grain species (Grossman 1972, Alexander & Ferguson 1994, Allard et al 1998). At each temperature, the fictitious pressure P_C of each condensed phase under consideration is calculated from the partial pressures of the species i which form the condensate (e.g. Al and O for corundum Al_2O_3) $P_i = N_i \mathcal{R} T$, where N_i is the number of moles of species i and $\mathcal{R}$ is the gas constant, determined by the vapour phase equilibria. This fictitious pressure

P_C is compared to the equilibrium pressure P_{eq}, calculated from the Gibbs energy of formation of the condensate. The abundance of a condensed species is determined by the condition that this species be in equilibrium with the surrounding gas phase, $P_C \geq P_{eq}$ (Grossman 1972). The opacities of the grains are calculated from Mie theory. As suggested by Fegley & Lodders (1996) and Allard et al (1998), refractory elements Al, Ca, Ti, Fe, and V are removed from the gaseous atmosphere by grain condensation at about the corundum (Al_2O_3) or perovskite ($CaTiO_3$) condensation temperature $T \lesssim 1800$ K. Rock-forming elements (Mg, Si, Fe) condense as iron and forsterite (Mg_2SiO_4) or enstatite ($MgSiO_3$) within about the same temperature range (depending on P). Therefore the spectral features of all these elements will disappear gradually for objects with T_{eff} below these temperatures (see e.g. Fegley & Lodders 1994, 1996; Lodders 1999; Burrows & Sharp 1999 for detailed calculations). For jovian-type effective temperatures ($T_{eff} \sim 125$ K), H_2O and NH_3 condense near and below the photosphere, and water and ammonia bands disappear completely for $T_{eff} \lesssim 150$ K and 80 K, respectively (Guillot 1999).

The gas abundance strongly depends on pressure and temperature, so that the abundances of various species vary significantly with the mass (and T_{eff}) of the astrophysical body. As shown e.g. in Figure 2 of Lodders (1999), the condensation point of the dominant clouds lies much closer to the photosphere for M-dwarfs than for Gl229B or—worse—for Jupiter. In other words, the location of a given grain condensation lies deeper in Jupiter than in Gl229B. For late M-dwarfs and for massive and/or young BDs, the main cloud formation is predicted to occur very near the photosphere. This is consistent with the fact that all the DENIS and 2MASS objects discovered near the bottom of and below the MS exhibit strong thermal heating and very red colors (Delfosse et al 1998b, Kirkpatrick et al 1999a; see Section 4.5.2). Indeed, the atmospheric heating resulting from the large grain opacity (the so-called greenhouse or backwarming effect), along with the resulting enhanced H_2O dissociation, yield a redistribution of the IR flux, as proposed initially by Tsuji et al (1996).

A key question for the grain formation process is the size of the grains (see e.g. Alexander & Ferguson 1994). The suppression of the flux in the optical in Gl229B suggests grain sizes of ~ 0.1 μm as a source of continuum opacity (Jones & Tsuji 1997, Griffith et al 1998), although the wings of alkali resonance lines (KI, NaI) are also a source of absorption in this region (Tsuji et al 1999, Burrows et al 2000). Recent calculations assume a grain-size distribution in the submicron range (Allard 1999). Inclusion of the grain absorption with this size distribution in the atmosphere of objects near the limit of the MS successfully reproduces the observed colors of GD 165B, Kelu-1 and of DENIS objects (Leggett et al 1998, Allard 1999, Goldman et al 1999, Chabrier et al 2000). However, the spectrum of GL229B shows no indication for dust in its IR spectrum from 1 to 5 μm (Allard et al 1996, Marley et al 1996, Tsuji et al 1996, Oppenheimer et al 1998, Schultz et al 1998). This suggests ongoing dynamical processes such as grain settling in SSO atmospheres. Indeed, as noted by Chabrier et al (2000), although convection

occurs only in optically-thick regions ($\tau > 1$) for L-dwarfs, the top of the convection zone lies only about one pressure-scale height or less below the photosphere ($\tau \sim 1$), close to the region where most grains condense for objects near the bottom of the MS. This can have important consequences on the mixing and the settling of atmospheric grains. Indeed although the temperature at the top of the convective zone is found to be generally above the condensation temperature of all grains, rotation-induced advection or turbulent diffusion could efficiently bring material upward to the region of condensation and maintain small-grain layers, which otherwise will settle gravitationally. In general, grain formation process involves a balance between various dynamical timescales, such as the condensation, evaporation, coagulation, coalescence, and convection timescales (see e.g. Rossow 1978), not to mention large-scale hydrodynamical instabilities, which are typical of weather conditions on Earth. See for example Marley et al (1999) for an early attempt at cloud modelling for BD and EGP atmospheres. Moreover, although to an excellent first approximation the atmosphere of the solar jovian planets are in thermodynamical equilibrium, non-equilibrium species with chemical equilibrium timescales larger than the convection timescale can be dredged up to the photosphere by convection, as e.g. CO, PH_3, GeH_4 in Jupiter (Fegley & Lodders 1994). A correct understanding and a reliable description of this complex grain formation process represent a major challenge for theorists, and the observation of spectra of SSOs over a significant temperature range is necessary to provide guidance through this maze.

2.2.2 Transport Properties   As mentioned previously, below ~ 5000 K—i.e. $m \sim 0.6$–$0.8\, M_\odot$ depending on the metallicity—hydrogen atoms recombine, and n_{H_2} increases, as does the opacity through H_2 CIA. The radiative opacity κ increases by several orders of magnitude over a factor 2 in temperature, which in turn decreases the radiative transport efficiency ($\mathcal{F}_{rad} \propto \frac{\nabla}{\kappa}$). On the other hand, the presence of molecules increases the number of internal degrees of freedom (vibration, rotation) and thus the molar specific heat C_p, which in turn decreases the adiabatic gradient $(dT/dP)_{ad} = \frac{\mathcal{R}}{C_p}\frac{T}{P}$. Both effects strongly favor the onset of convection in the optically-thin ($\tau < 1$) atmospheric layers (Copeland et al 1970, Allard 1990, Saumon et al 1994, Baraffe et al 1995) with a maximum radial extension for the convection zone around $T_{\text{eff}} \sim 3000$ K. The combination of relatively large densities, opacities, and specific heat in layers where H_2 molecules are present contributes to a very efficient convective transport. Convection is found to be adiabatic almost up to the top of the convective region, and the extension of the superadiabatic layers is very small compared to solar-type stars (Brett 1995, Allard et al 1997). Thus a variation of the mixing length between H_P and $2H_P$ barely affects the thermal atmospheric profile (Baraffe et al 1997; Section 3). The presence of convection in the optically thin layers precludes radiative equilibrium in the atmosphere ($\mathcal{F}_{tot} \neq \mathcal{F}_{rad}$) and requires the resolution of the transfer equation for radiative-convective atmosphere models for objects below $\sim 0.7\, M_\odot$. This and

the aforementioned strong frequency-dependence of the molecular absorption coefficients exclude grey model atmosphere and/or the use of radiative $T(\tau)$ relationships to determine the outer boundary condition to the interior structure. As demonstrated by Saumon et al (1994) and Baraffe et al (1995, 1997, 1998), such outer boundary conditions overestimate the effective temperature and the HBMM and yield erroneous m-T_{eff} and m-L relationships, two key relations for the calibration of the temperature scale and for the derivation of mass functions (see Chabrier & Baraffe 1997, Section 2.5 for a complete discussion). Correct evolutionary models for low-mass objects require (1) the connection between the non-grey atmospheric (P, T) profile, characterized by a given $(\log g, T_{\text{eff}})$ and the interior (P, T) profile at a given optical depth τ, preferably large enough for the atmospheric profile to be adiabatic; and (2) consistency between the atmospheric profiles and the synthetic spectra used to determine magnitudes and colors. For a fixed mass and composition, only one atmosphere profile matches the interior profile for the aforementioned boundary condition. This determines the complete stellar model (mass, radius, luminosity, effective temperature, colors) for this mass and composition (Chabrier & Baraffe 1997; Burrows et al 1997 for objects below 1300 K in their Figure 1).

2.3 Activity

The Einstein and Rosat surveys of the solar neighborhood and of several open clusters have allowed the identification of numerous M-dwarfs as faint X-ray sources, with typical luminosities of the order of the average solar luminosity $L_X \sim 10^{27}$ erg s^{-1}, reaching up to $\sim 10^{29}$ erg s^{-1} in young clusters (see e.g. Randich, 1999 and references therein for a recent review). This suggests that late M-dwarfs, as coronal emitters, are as efficient as other cool stars in terms of L_X/L_{bol}, which expresses the level of X-ray activity. Moreover, about 60% of M-dwarfs with spectral-type $>M5$ ($M_{\text{bol}} \simeq 12$) show significant chromospheric activity with $\log(L_{H\alpha}/L_{bol}) \simeq -3.9$ (Hawley et al 1996). These observations provide important empirical relationships between age, rotation, and activity. The L_X/L_{bol} ratio seems to saturate above a rotational velocity threshold at a limit $\log(L_X/L_{bol}) \simeq -3$, implying that the intrinsic coronal emission of LMS and BDs is quite low and decreases with L_{bol}, and thus mass, and does not increase with increasing rotation above the threshold limit. This suggests a saturation relation in terms of a Rossby number, i.e. the ratio of the rotational period over the convective turnover time $Ro = \frac{P}{t_{conv}}$ (see Section 2.1.3). Because t_{conv} increases for lower-mass stars, they will saturate at progressively larger periods, i.e. lower rotational velocities. The velocity threshold for a 0.4 $M_\odot$ star is estimated around 5–6 km s^{-1} (Stauffer et al 1997). Comparison of the Pleiades and the Hyades samples shows a steep decay of the X-ray activity in the Hyades. This result is at odds with a simple, monotonic rotation-activity relationship. The spin-down timescales for M-dwarfs are much longer than for solar-type stars. Hyades

M-dwarfs do indeed show moderate or even rapid rotation ($v \sin i \geq 10$ km s^{-1}) and thus should show strong X-ray emission. The fainter L_X in the Hyades than in the Pleiades thus reinforces the saturation scenario.

Delfosse et al (1998a) obtained projected rotational velocities and fluxes in the H$_\alpha$ and H$_\beta$ lines for a volume-limited sample of 118 field M-dwarfs with spectral-type M0–M6. They found a strong correlation between rotation and both spectral type (measured by $R - I$ colors) and kinematic population: All stars with measurable rotation are later than M3.5 and have kinematic properties typical of the young disk population, or intermediate between young disk and old disk. They interpret this correlation as evidence for a spin-down timescale that increases with decreasing mass, and this timescale is a significant fraction of the age of the young disk ($\sim$3 Gyr) at spectral type M4 ($\sim$0.15 $M_\odot$). These data confirm the saturation relation inferred previously for younger or more massive stars: L_X/L_{bol} and L_{H_α}/L_{bol} both correlate with $v \sin i$ for $v \sin i \lesssim$4–5 km s^{-1} and then saturate at $10^{-2.5}$ and $10^{-3.5}$, respectively. Recently, Neuhäuser & Comeron (1998) detected X-ray activity in young BDs with $m \approx 0.04 M_\odot$ in the Chamaleon star-forming region, with $\log L_X = 28.41$ and $\log L_X/L_{bol} = -3.44$. Coronal activity in BDs has been confirmed by Neuhäuser et al (1999), with all the objects belonging to young clusters or star-forming regions.

All these observations show that there is no drop in L_X/L_{bol} in field stars up to a spectral type of $M7$, which is well below the limit $m \sim 0.3 M_\odot$ where stellar interiors are predicted to become fully convective. However, recent observations of the 2MASS objects (Kirkpatrick et al, 1999a: Figure 15a) seem to show a significant decrease of activity for L-type objects, which confirms the decline of activity suggested previously for very late M-spectral types ($\gtrsim$M8) (Hawley et al 1996, Tinney & Reid 1998). In any event, X-ray emission does not disappear in fully convective stars, and even at least young SSOs can support magnetic activity. A fossil field can survive only over a timescale $\tau_d \approx R^2/\eta \sim$ a few years for fully convective stars ($\eta \equiv \eta_t$ is the turbulent magnetic diffusivity and R the stellar radius), so that a dynamo process is necessary to generate the magnetic field. The data suggest that (1) the dynamo-generation believed to be at work in the Sun does not apply for very-low-mass objects, (2) dynamo generation in fully convective stars is as efficient as in stars with a radiative core, and (3) whatever the dynamo mechanism is, it is bounded by the saturation condition at least for late-type stars.

It is generally admitted that magnetic activity in the Sun results from the generation of a large-scale toroidal field by the action of differential rotation on a poloidal field at the interface between the convective envelope and the radiative core—where differential rotation is strongest—known as the tachocline (Spiegel & Weiss 1980, Spiegel & Zahn 1992). In this region, a sufficiently strong magnetic field is stable against buoyancy. In this case the shear dominates the helicity; this is the so-called $\alpha\Omega$ dynamo-generation, which predicts a correlation between activity and rotation, as observed in solar-type stars.

As shown initially by Parker (1975), buoyancy prevents the magnetic field generated by the turbulent motions in a convective zone to become global in character. For this reason, the absence of a radiative core—i.e. of a region of weak buoyancy and strong differential rotation—precludes in principle the generation of a large-scale magnetic field. A dynamo generated by a turbulent velocity field that would generate chaotic magnetic fields in the absence of rotation has been proposed as an alternative process for fully convective stars (Durney et al 1993). They found that a certain level of magnetic activity can be maintained without the generation of a large-scale field. The turbulent velocity field can generate a self-maintained *small-scale* magnetic field, providing that the magnetic Reynolds number $Re = (vl/\eta)^2$ is large enough. The scale of this field is comparable to that of turbulence and is in rough energy equipartition with the fluid motions, i.e. $\frac{1}{8\pi}\langle(B_P^2 + B_\phi^2)\rangle \approx \frac{1}{2}\langle\rho v_{conv}^2\rangle$. Rotation is not essential in this case, but it increases the generation rate of the field.

Recently, Küker and Chabrier (in preparation) explored an other possibility, namely the generation of a *large-scale* field by a pure α^2-effect. In the α^2-dynamo, helicity is generated by the action of the Coriolis force on the convective motions in a rotating, stratified fluid. The α^2-effect strongly depends on the Rossby number, or the equivalent Coriolis number $\Omega^\star = 2t_{conv}\Omega = 4\pi/Ro$. In low-mass objects, the convective turnover time is longer than the rotation period (see Section 2.1.3), so that $\Omega^\star \gg 1$. They find that the α^2-dynamo is clearly supercritical. It generates a large-scale, non-axisymmetric steady (co-rotating) field that is symmetric with respect to the equatorial plane. Equipartition of energy yields field strengths of several kiloGauss. The possible decrease of activity in very late-type stars, as observed for example with the small chromospheric activity of the M9.5 BD candidate BRI 0021-0214 in spite of its fast rotation ($v \sin i = 40\,\mathrm{km\,s^{-1}}$; Tinney et al 1998), is a more delicate issue that requires the inclusion of dissipative processes. Indeed, these calculations show that α^2-dynamo can efficiently generate a large-scale magnetic field in the interior of fully convective stars. Since conductivity decreases in the outermost layers of the star, however, no current would be created by the field in these regions, and thus no dissipative process and no activity (see e.g. Meyer & Meyer-Hofmeister 1999).

The observed continuous transition in rotation and activity at the fully convective boundary suggests in fact that the α^2-dynamo is already at work in the convection zones of the more massive stars. An interesting possibility for verifying the present theory would be Doppler imaging of fast-rotating LMS and BDs. Turbulent dynamo is likely to yield a spatially uniform chromospheric activity, whereas the large-scale α^2 process suggested by Küker & Chabrier generates asymmetry. Moreover, non-axisymmetric fields can propagate in longitudinal directions without any cyclic variation of the total field energy, whereas dynamo waves generated by $\alpha\Omega$ processes propagate only along the lines of constant rotation rate (Parker 1955). Therefore, we do not expect cycles for uniformly rotating (fully convective) stars.

3.   MECHANICAL AND THERMAL PROPERTIES

3.1   Mechanical Properties

Figure 3 portrays the mass-radius behavior of LMS and isolated SSOs from the Sun to Jupiter for $t = 6 \times 10^7$ (*dot-dash line*) and 5×10^9 yr (*solid line*) for $Z = Z_\odot$ and $Z = 10^{-2} \times Z_\odot$ (*dashed-line*). The time required to reach the ZAMS, arbitrarily defined as the time when $L_{nuc} = 95\%\, L_{tot}$, for solar metallicity LMS is given in Table 1.

The general *m-R* behavior reflects the physical properties characteristic of the interior of these objects, as inferred from Figure 1. For $m \gtrsim 0.2\ M_\odot$, $\psi > 1$ for all ages, so that the internal pressure is dominated by the classical perfect
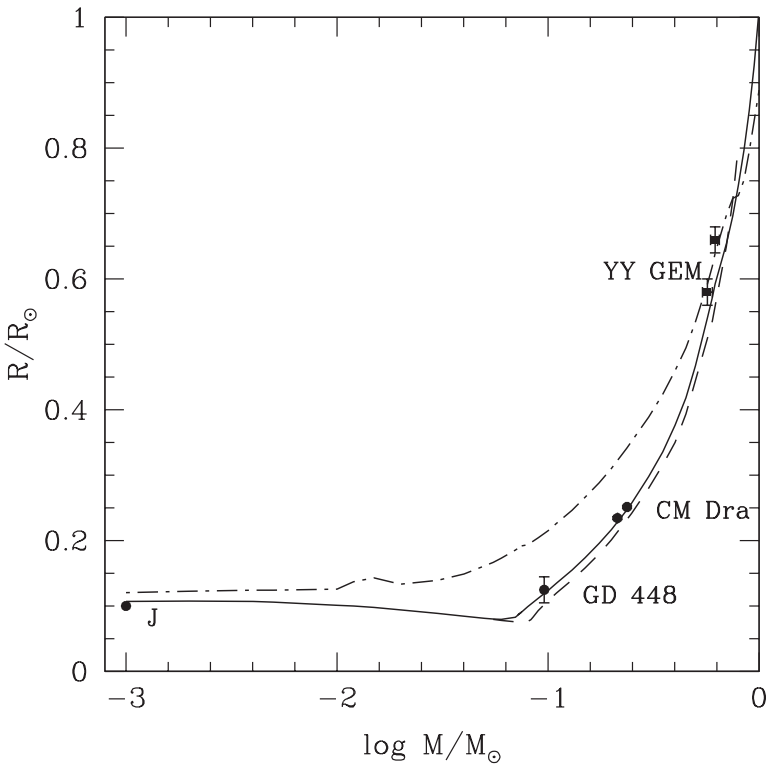
Figure 3   Mass-radius relationship for LMS and SSOs for two ages, $t = 6 \times 10^7$ yr (*dot-dash line*), 5×10^9 yr (*solid line*) for $Z = Z_\odot$, and $t = 5 \times 10^9$ yr for $Z = 10^{-2} \times Z_\odot$ (*dashed line*). The HBMM is 0.075 $M_\odot$ for $Z = Z_\odot$ and 0.083 $M_\odot$ for $Z = 10^{-2} \times Z_\odot$. Also indicated are the observationally-determined radii of various objects (see text) and the position of Jupiter radius (J). The bump on the 6×10^7 yr isochrone illustrates the initial D-burning phase.

TABLE 1   ZAMS age for solar metallicity LMS (after Baraffe et al 1998)

$m/M_\odot$	0.075	0.08	0.09	0.1	0.2	0.4	0.6	0.8	1
t_{ZAMS} (Gyr)	3	1.7	1	0.7	0.33	0.20	0.12	0.06	0.04

gas ion+electron contribution ($P = \rho kT/\mu m_H$, neglecting the molecular rotational/vibrational excited level contributions), plus the correcting Debye contribution arising from ion and electron interactions ($P_{DH} \propto -\rho^{3/2}/T^{1/2}$) and $R \propto m$ in first order from hydrostatic equilibrium. When the density becomes large enough during pre-MS contraction so that $\psi < 1$, which occurs at t $\gtrsim$ 50 Myr for $m = 0.15\,M_\odot$ and at t $\gtrsim$ 10 Myr for the HBMM $m = 0.075\,M_\odot$, the EOS starts to be dominated by the contribution of the degenerate electron gas ($P \propto \rho^{5/3}$). This yields a minimum in the m-R relationship $R_{min} \approx 0.08R_\odot$ for $m \sim 0.06$–$0.07\,M_\odot$. Full degeneracy ($\psi \simeq 0$) would yield the well-known zero-temperature relationship $R \propto m^{-1/3}$, as in white dwarf interiors, but partial degeneracy and the non-negligible contribution arising from the (classical) ionic Coulomb pressure (which implies $R \propto m^{+1/3}$) combine to yield a smoother relation $R = R_0 m^{-1/8}$ at t $=$ 5 Gyr, where $R_0 \simeq 0.06\,R_\odot$ for $0.01\ M_\odot \lesssim m \lesssim 0.07\,M_\odot$, i.e. an almost constant radius. For the age and metallicity of the solar system, this radius is of the order of the Jupiter radius $R_J \simeq 0.10 \times R_\odot$. At 5 Gyr, the radius reaches a maximum $R \simeq 0.11\,R_\odot$ for $m \simeq 4 \times M_J$ (where $M_J = 9.5 \times 10^{-4}\,M_\odot$ is the Jupiter mass) (Zapolsky & Salpeter 1969, Hubbard 1994, Saumon et al. 1996). Below this limit, degeneracy saturates (see Figure 1) and the classical ionic pressure contribution becomes important enough so that we recover a nearly classical behavior. Figure 3 also displays the astrophysically determined radii of the two eclipsing binary systems YY-Gem (Leung & Schneider 1978) and CM-Dra (Metcalfe et al 1996), and of the white dwarf companion GD448 (Maxted et al 1998). The bump on the 60 Myr isochrone near $m \sim 0.01M_\odot$ results from initial deuterium burning (see Section 3.2). The m-R relationship is essentially determined by the EOS and is weakly sensitive to the outer boundary condition and the structure of the atmosphere, since the latter represents at most (for 1 $M_\odot$) a few percent of the total radius of LMSs and SSOs (Dorman et al 1989, Chabrier & Baraffe 1997). The effect of metallicity Z on the m–R relation remains modest. A decrease in metallicity yields a slight decrease in the radius at a given age or at the same stage of nuclear burning (i.e. the same H content). Indeed, lower metallicity yields a larger T_{eff} at a given mass (see Section 3.2). This in turns implies an increase in the nuclear energy production to reach thermal equilibrium, and thus a larger central temperature T_c. Since $R \propto \mu m/T$ from hydrostatic equilibrium, where μ is the mean molecular weight, determined essentially by hydrogen and helium, a lower-metallicity star contracts more to reach thermal equilibrium. As shown by Beuermann et al (1998), the variation of R with Z predicted by the models of Baraffe et al (1998) is in agreement with the radii deduced from observations.

3.2   Thermal Properties

Figure 4 exhibits the mass-effective temperature relationships for representative ages and metallicities. The arrows indicate the onset of formation of H_2 near the photosphere (Auman 1969, Copeland et al 1970, Kroupa et al 1990). As discussed in Section 2.2.2, molecular recombination favors convective instability in the atmosphere. Convection yields a smaller T-gradient ($\nabla \sim \nabla_{ad}$) and thus a cooler structure in the deep atmosphere (Brett 1995, Allard & Hauschildt 1995, Chabrier & Baraffe 1997; Figure 5). Therefore, a model with atmospheric convection corresponds to a larger T_{eff} since the (P, T) interior-atmosphere boundary is fixed for a given mass (Section 2.2.2). Furthermore, the adiabatic gradient in the regions of H_2 recombination decreases to a minimum value $\nabla_{ad} \sim 0.1$, compared to $\nabla_{ad} \sim 0.4$ for an ideal monoatomic gas (Copeland et al 1970, Saumon et al 1995: Figure 17). Therefore, even if the atmosphere were already convective without
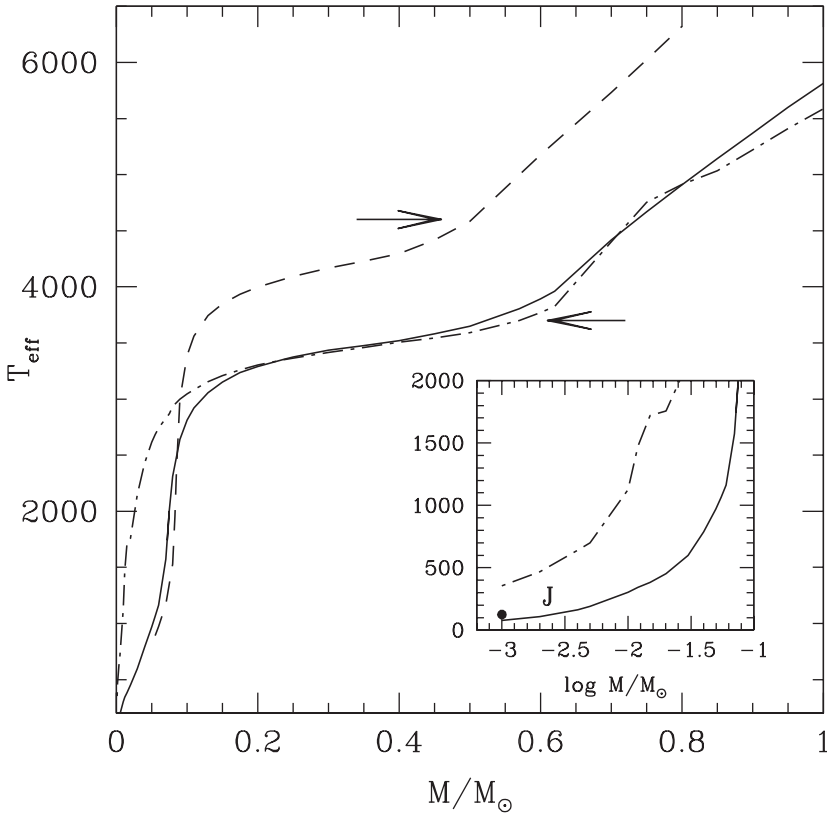

Figure 4   Mass-T_{eff} relationship for LMS and SSOs. Same legend as in Figure 3. The arrows indicate the onset of H_2 formation near the photosphere. Note the log scale in the inset.

H_2, molecular recombination yields a flatter inner temperature gradient in the atmosphere and thus enhances the former effect, i.e. a larger T_{eff} for a given mass. Formation of H_2 in the atmosphere occurs at higher T_{eff} for decreasing metallicity, because of the denser (more transparent) atmosphere (see Figure 4). The relation between the central and effective temperatures for LMS and SSOs can be inferred from Figures 1 and 4 and is commented on by Chabrier & Baraffe (1997; Section 4.2) and Baraffe et al. (1998; Section 2). As these authors demonstrate, a grey approximation or the use of a radiative $T(\tau)$ relationship significantly overestimates the effective temperature (from ~50 to 300 K depending on the atmospheric treatment).

A representative T_c-ρ_c diagram is shown in Figure 5 (see also Figure 8 of Burrows et al 1997) and illustrates the different evolutionary paths for LMS and SSOs in this diagram. The bumps appearing on the isochrones between 10^6 and 10^8 yr and $\log T_c \sim 5.4$–5.8 result from initial deuterium burning. For
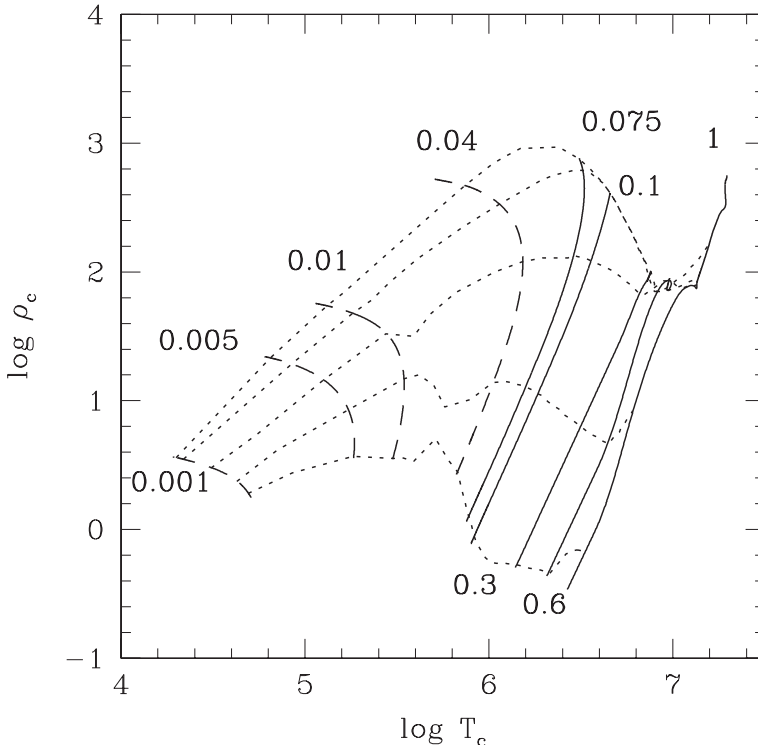

Figure 5 T_c-ρ_c relationship (in cgs) for LMS (*solid lines*) and SSOs (*dashed lines*) from 1 $M_\odot$ to 0.001 $M_\odot$ (masses in $M_\odot$ indicated on the curves). (*Dotted lines*) represent 10^6, 10^7, 10^8, 10^9, and 5 10^9 yr isochrones from bottom to top. The bumps on the 10^6–10^8 yr isochrones at $\log T_c \sim 5.4$–5.8 correspond to the initial deuterium burning phase.

stars, T_c and ρ_c always increase with time until they reach the ZAMS. For BDs, T_c first increases for $\sim 10^7$–10^9 yr, for masses between ~ 0.01 and $\sim 0.07\ M_\odot$, respectively. Then, when degeneracy becomes dominant, T_c reaches a maximum and decreases. For objects with m $\lesssim 5 \times 10^{-3}\ M_\odot$, T_c always decreases for $t \gtrsim 1$ Myr. In the substellar regime there is no steady nuclear energy generation, by definition, and the evolution is governed by the change of internal energy $\int_M \frac{dE}{dt}\, dm$ and the release of contraction work $\int_M \frac{P}{\rho^2} \frac{d\rho}{dt}\, dm$. Even when degeneracy becomes important, SSOs keep contracting, though very slowly, within a Hubble time.

4.   EVOLUTION

4.1   Evolutionary Tracks

Figure 6 exhibits $T_{\mathrm{eff}}(t)$ obtained from consistent non-grey calculations for several masses, for [M/H][1] $= 0$ (helium mass fraction $Y = 0.275$) and [M/H] $= -2.0$ ($Y = 0.25$), respectively. Initial deuterium burning (with an initial mass fraction $[D]_0 = 2 \times 10^{-5}$) for masses m $\gtrsim 0.013\ M_\odot$ proceeds quickly at the early stages of evolution and lasts about $\sim 10^6$–10^8 years. Objects below this limit are not hot enough to fuse deuterium in their core (see Figure 2). For masses above $0.07\ M_\odot$ for $[M/H] = 0$ and $0.08\ M_\odot$ for $[M/H] = -2.0$, the internal energy provided by nuclear burning quickly balances the gravitational contraction energy, and after a few Gyr the lowest-mass star reaches complete thermal equilibrium ($L = \int \epsilon_{\mathrm{nuc}}\, dm$, where ϵ_{nuc} is the nuclear energy rate) for both metallicities. The lowest mass for which thermal equilibrium is reached defines the HBMM and the related hydrogen-burning minimum luminosity HBML. Stars with $m \geq 0.4\ M_\odot$ develop a convective core near the ZAMS for a relatively short time (depending on the mass and metallicity), which results in the bumps for 0.6 and 1 $M_\odot$ at $\sim 10^8$ yr and $\sim 3 \times 10^7$ yr, respectively (Chabrier & Baraffe 1997; Section 3.2). The dotted lines portray $T_{\mathrm{eff}}(t)$ for objects with solar abundance when grain opacity is taken into account in the atmosphere (see Section 4.5.2). The Mie opacity resulting from the formation of refractory silicate grains produces a blanketing effect that lowers the effective temperature and luminosity at the edge of the main sequence, an effect first noticed by Lunine et al (1989). However, as a whole, grain formation only moderately affects the evolution near and below the bottom of the main sequence and thus the HBMM and HBML. Models with grainless atmospheres yield $m = 0.072\ M_\odot$, $L = 5 \times 10^{-5}\ L_\odot$, and $T_{\mathrm{eff}} = 1700$ K at the H-burning limit, whereas models with grain opacity give $m = 0.07\ M_\odot$, $L = 4 \times 10^{-5}\ L_\odot$ and $T_{\mathrm{eff}} = 1600$ K, for solar composition (Chabrier et al 2000). As shown in Figure 6, young and massive BDs can have the same effective temperature (or luminosity) as older, very-low-mass stars, a possible source of contamination for
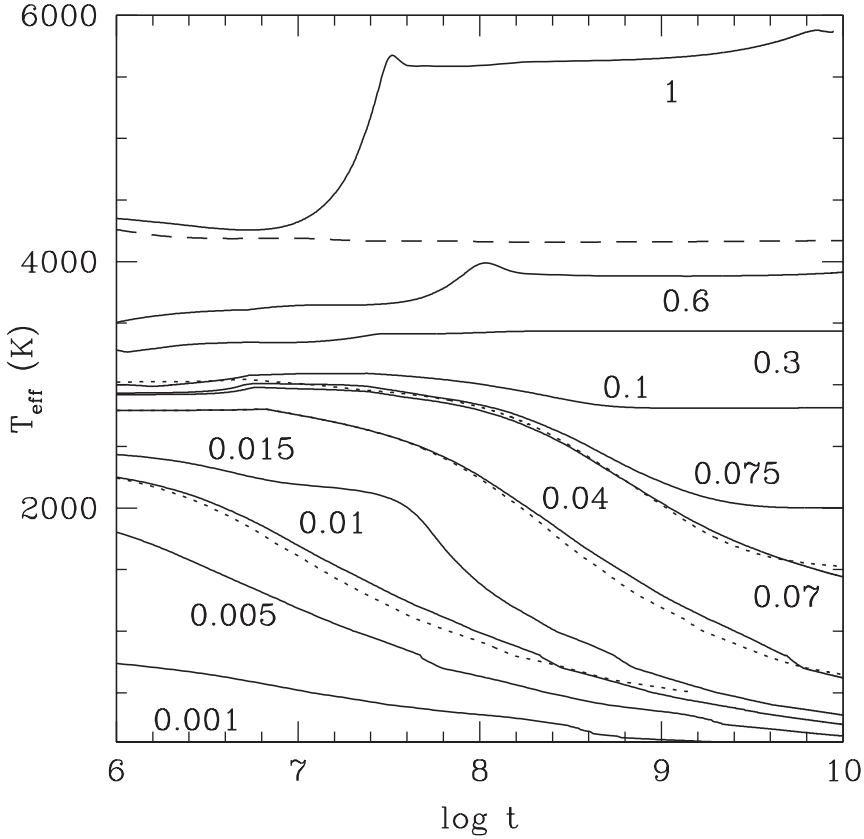
---

[1][M/H] $= \log (Z/Z_\odot)$.

Figure 6 Effective temperature versus time (yr) for objects from 1 $M_\odot$ to 10^{-3} $M_\odot$ (masses indicated in $M_\odot$). (*Solid lines*): $Z = Z_\odot$, no dust opacity; (*dotted lines*): $Z = Z_\odot$, dust opacity included, shown for 0.01, 0.04, and 0.07 $M_\odot$; (*dashed line*): $Z = 10^{-2} \times Z_\odot$ (only for 0.3 $M_\odot$).

the determination of the local stellar luminosity function at the bottom of the MS (see Section 5).

Note the quick decrease of $T_{\rm eff}$ (and L) with time for objects below the HBMM, $L \propto t^\alpha$ with $\alpha \sim -5/4$ (Stevenson 1991; Burrows et al 1994, 1997), with a small dependence of α on the presence of grains. Slightly below ~ 0.072 $M_\odot$ (resp. 0.083 $M_\odot$) for $[M/H] = 0$ (resp. $[M/H] \leq -1$), nuclear ignition still takes place in the central part of the star, but cannot balance the ongoing gravitational contraction (see Figure 2). Although these objects are sometimes called "transition objects," we prefer to consider them as massive BDs, because strictly speaking they will never reach thermal equilibrium. Indeed, just below the HBMM, the contributions from the nuclear energy source $\int \epsilon_{\rm nuc} \, dm$ and the entropy source $\int T \frac{dS}{dt} \, dm$ are comparable, and cooling proceeds at a much slower rate than mentioned above.

Below about 0.07 $M_\odot$ (resp. 0.08 $M_\odot$) for [M/H] = 0 (resp. [M/H] ≤ -0.5), the energetic contribution arising from hydrogen-burning, though still present for the most massive objects, is orders of magnitude smaller than the internal heat content, which provides essentially all the energy of the star ($\epsilon_{\mathrm{nuc}} \ll T|\frac{dS}{dt}|$). Once on the ZAMS the radius for stars is essentially constant, whereas for BDs the contraction slows down when $\psi \lesssim 0.1$ (see Figures 1 and 3).

The effects of metallicity on the atmosphere structure (Brett 1995, Allard and Hauschildt 1995) and on the evolution (Saumon et al 1994, Chabrier & Baraffe 1997) have been discussed extensively in the previously cited references and can be apprehended with simple arguments: the lower the metallicity Z, the lower the mean opacity $\bar{\kappa}$ and the more transparent the atmosphere, so that the same optical depth lies at deeper levels and thus higher pressure ($\frac{dP}{d\tau} = \frac{g}{\bar{\kappa}}$). Therefore, for a given mass (log g) the (T, P) interior profile matches, for a given optical depth τ, an atmosphere profile with larger T_{eff} (dashed-line on Figure 4), and thus higher luminosity L since the radius depends only weakly on the metallicity. The consequence is a larger HBMM for lower Z because a larger L requires more efficient nuclear burning to reach thermal equilibrium, and thus a larger mass.

A standard way to display evolutionary properties is a theoretical Hertzsprung-Russell diagram (HRD). Such an HRD for LMS and SSOs is shown in Figure 7 for several masses and isochrones from 1 Myr to 5 Gyr, whereas Figure 8 shows evolutionary tracks in a log g-T_{eff} diagram (see also Burrows et al 1997). These figures allow the determination of the mass and age of an object from the gravity and effective temperature inferred from its spectrum.

4.2 Mass-Magnitude

One of the ultimate goals of stellar theory is an accurate determination of the mass of an object for a given magnitude and/or color. Figure 9 (see color insert; see also Baraffe et al 1998) shows the comparison between theory and observationally-determined masses in the K-band. The solid line corresponds to a 5×10^9 yr isochrone, for which the lowest-mass stars have settled on the MS, for a solar metal-abundance ([M/H] = 0), whereas the dotted line corresponds to a 10^8 yr isochrone for the same metallicity, and the dashed line corresponds to a 10^{10} yr isochrone for [M/H] = -0.5, which is representative of the thick-disk population. A striking feature is the weak metallicity-dependence in the K-band, compared with the strong dependence in the V-band (see Figure 3 of Baraffe et al 1998). As we discuss in this chapter, this stems from two different effects. On one hand, the increasing opacity in the optical, dominated by TiO and VO lines, and the decreasing H_2 opacity in the K-band with increasing metallicity shift the peak of the flux toward larger wavelengths. Thus, for fixed T_{eff} the V-flux decreases and the K-flux increases with increasing [M/H]. On the other hand, for a given mass, the total flux (and T_{eff}) decreases with increasing metallicity, as we mentioned in Section 4.1. These two effects add up in the V-band and yield an important variation of the V-flux with metallicity. In the K-band, they cancel and yield similar fluxes
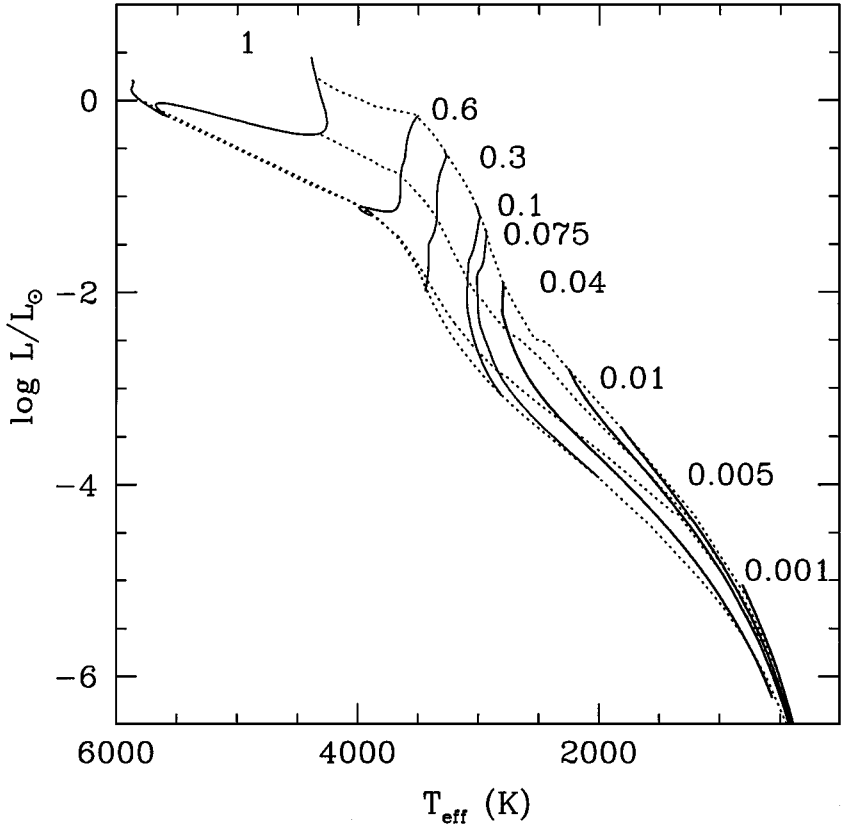
Figure 7   Theoretical H-R diagram for various masses (labeled in $M_\odot$). The weak dependence of radius on mass for SSOs yields the merging of the tracks for the lowest-mass objects. (*Dotted lines*) represent 10^6, 10^7, 10^8, and $5\ 10^9$ yr isochrones from right to left. The models are calculated with a mixing length $l = 1.9\ H_{\rm P}$.

for a given mass below $\sim 0.4\ M_\odot$ ($T_{\rm eff} \sim 3500$–4300 K, depending on [M/H]) at different metallicities. These arguments remain valid as long as H_2 CIA does not significantly depress the K-band, as it does for very metal-depleted objects.

4.3   Mass-Spectral Type

The knowledge of spectral type (Sp) is extremely useful for analyzing objects with unknown distance or with colors altered by reddening, as in young clusters, for example. The determination of a mass-Sp relationship provides a powerful complement to the mass-magnitude relationship for assigning a mass to an object. Based on spectroscopic observations of low-mass nearby composite systems, Kirkpatrick & McCarthy (1994) have determined an empirical m-Sp relationship for M-dwarfs, restricted to M2–M6 spectral types. A theoretical relation has been
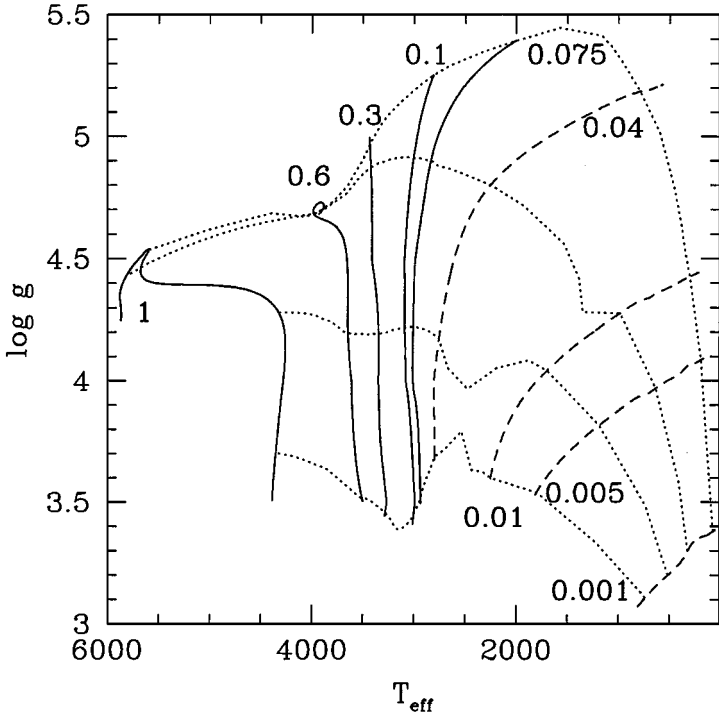
Figure 8 log g (in cgs) versus T_{eff} (in K) for LMS (*solid curves*) and SSOs (*dashed curves*) from 1 $M_\odot$ to 0.001 $M_\odot$ (masses in $M_\odot$ indicated on the curves). *Dotted lines* represent 10^6, 10^7, 10^8, and 5 10^9 yr isochrones from bottom to top.

derived by Baraffe & Chabrier (1996) from M0 to M10, emphasizing the non-linear behavior of this relationship near the bottom of the MS, for >M6. Figure 10 (see color insert) shows the *m-Sp* relationship for M-, K-, and G-dwarfs based on the Baraffe et al (1998) models. The spectral type for K- and G-dwarfs is derived from the model synthetic color $(I - K)$ through the empirical $Sp(I - K)$ relation recently derived by Beuermann et al (1998). As Baraffe & Chabrier (1996) stress, the *m-Sp* relationship depends crucially on age and metallicity. At ∼1 Gyr, objects with *Sp* later than M10 are below the HBMM and can be considered as bona-fide BDs. This limit decreases to ∼M7 at 100 Myr and ∼M6 at 10 Myr. A difficulty arises when we're dealing with very young objects ($t \lesssim 10$ Myr) because of gravity effects. No reliable *Sp*-color relationship is presently available for the objects for which spectroscopic and photometric properties are found to be intermediate between giants and dwarfs (Luhman 1999). The present *m-Sp* relationships should be extended in the future to dwarfs cooler than M9.5–M10, the so-called L-dwarfs and methane-dwarfs. Note, however, that SSOs evolve at different rates through a series of spectral types as they cool, so we cannot associate a given spectral type with a specific mass for these objects.

4.4 Irradiated Planets

The mass-radius relation and evolutionary sequences described above reflect the relations for isolated objects. After a rapid initial accretion phase and subsequent hydrodynamical collapse, planets orbiting stars will evolve differently. As shown by Hubbard (1977) illumination from a parent star will yield thermal expansion of the less massive (low gravity) objects, toward an asymptotic temperature T_{eq} set only by the thermalized photons from the parent star and toward a (larger) asymptotic equilibrium radius R_p, with $R_p = 2a(L_{eq}/L_\star)^{1/2}[1/(1-A)]^{1/2}$ and $T_{eq} = (1-A)^{1/4}(R_\star/2a)^{1/2}T_{eff_\star}$, where a is the orbital distance, A is the Bond albedo, $L_\star = 4\pi\sigma R_\star^2 T_{eff_\star}$ is the parent star luminosity, effective temperature, and radius, and $L_{eq} = 4\pi\sigma R_p^2 T_{eq}^4$ denotes the equilibrium luminosity (see Saumon et al 1994). As noted in Guillot et al (1996) and Guillot (1999), EGPs in close orbits are heated substantially by their parent star, and their atmosphere cannot cool substantially. They develop an inner radiative region as a result of this stellar heating and contract at almost constant T_{eff}, at a much smaller rate than if they were not heated by the star. Planets whose luminosity is larger than the absorbed stellar flux of the parent star just evolve along a fully convective Hayashi track for $\sim 10^6$ yr before reaching the aforementioned equilibrium state.

The flux from an irradiated planet includes two contributions: the intrinsic thermal emission and the reflected starlight (the Albedo contribution) (see e.g. Seager & Sasselov 1998, Marley et al 1999):

$$F_\nu = \left(\frac{R_p}{d}\right)^2 \mathcal{F}_\nu^p + \left(\frac{A}{4}\right) P(\phi) \left(\frac{R_\star}{d}\right)^2 \left(\frac{R_p}{a}\right)^2 \mathcal{F}_\nu^\star, \qquad (5)$$

where d is the distance of the system to Earth, and $P(\phi)$ is the dependence of the reflected light upon the phase angle between the star, the planet, and Earth ($P = 1$ if the light reflected by the planet is redistributed uniformly over 4π steradians). Figure 11 (see color insert) illustrates the flux from a young EGP (assuming the irradiation is isotropic) with $T_{eff} = 1000$ K orbiting a Sun-like star at 15 pc for various orbital distances.

4.5 Color-Magnitude Diagrams

Thanks to the recent progress both on the observational side, with the development of several ground-based and space-based observational surveys of unprecedented sensitivity in various optical and infrared passbands, and on the theoretical side, with the derivation of synthetic spectra and consistent evolutionary calculations based on non-grey atmosphere models, it is now possible to confront theory with observation directly in the observational planes, i.e. in color-color and color-magnitude diagrams (CMD). This avoids dubious color-T_{eff} or color-M_{bol} transformations and allows more accurate determinations of the intrinsic properties (m, L, T_{eff}, R) of an object from its observed magnitude and/or color.

In this section we examine the behavior of LMS and SSOs in various CMDs characteristic of different populations in terms of age and metallicity. These diagrams capture the essence of the observational signatures of the very mechanical and thermal properties of these objects, described in the previous sections.

4.5.1 Pre-Main Sequence and Young Clusters   Numerous surveys devoted to the detection of SSOs have been conducted in young clusters with ages spanning from $\sim$1–10 Myr to $\gtrsim 10^8$ yr for the Pleiades or the Hyades (see Martín 1999 and Basri, this volume, for reviews). Observations of young clusters present two important advantages, namely (1) all objects in the cluster are likely to be coeval within a reasonable range, except possibly in star-forming regions, where the spread in ages for cluster members can be comparable with the age of the cluster; and (2) young objects are brighter for a given mass (see Figure 6), which makes the detection of very-low mass objects easier. Conversely, they present four major difficulties: (1) extinction caused by the surrounding dust modifies both the intrinsic magnitude and the colors of the object; (2) accurate proper motion measurements are necessary to assess whether the object belongs to the cluster; (3) gravity affects both the spectrum and the evolution; and (4) the evolution and spectrum of very young objects ($t \lesssim 1$ Myr) may still be affected by the presence of an accretion disk or circumstellar material residual from the protostellar stage. Young multiple systems remove some of these difficulties and provide excellent tests for models at young ages—for example, the quadruple system GG TAU (White et al 1999), with components covering the whole mass-range of LMS and BDs from 1 $M_\odot$ to $\sim$0.02 $M_\odot$. Models based on non-grey atmospheres (Baraffe et al 1998) are the only ones consistent with these observations (White et al 1999, Luhman 1999). The comparison of $\sim$$10^6$ yr isochrones for SSOs with observations in a near-IR CMD is shown in Zapatero Osorio et al (1999) for the young cluster σ-Orionis (their Figure 1).

4.5.2 Disk Field Stars   Figure 12 and 13 (see color insert) display the CMDs for LMS and SSOs in the optical and the infrared for various ages and metallicities (see also Burrows et al 1997). Various sets of models correspond to calculations where (1) grain formation is included in the atmosphere EOS but not in the transfer equations, mimicking a rapid settling below the photosphere (COND models); (2) grain formation is included in both the EOS and the opacity (DUSTY models) (see Allard et al 1999); and (3) grainless models. Models (1) and (2) represent extreme cases that bracket the complex grain processes at play in these atmospheres (see Section 2.2.1). The optical sequence shows a monotonic magnitude-color behavior with three changes of slope around $M_V \sim 10$, 13, and 19 for $Z = Z_\odot$, respectively, which correspond to 0.5 $M_\odot$, $T_{eff} = 3600$ K; 0.2 $M_\odot$, $T_{eff} = 3300$ K, and 0.08 $M_\odot$, $T_{eff} = 2330$ K on the 5 Gyr isochrone. They reflect, respectively, the onset of convection in the atmosphere, degeneracy in the core, and grain absorption near the photosphere, as described in the previous sections. The latter feature, which yields a steep increase of M_V at $(V - I) \sim 5$, does not appear in dust-free

models (cf Baraffe et al 1998), where TiO is not depleted by grain formation in the atmosphere and thus absorbs the flux in the optical. It is interesting that this steepening is observed in the sample collected recently by Dahn et al (1999), which includes some DENIS and 2MASS L-dwarf parallaxes. This effect is also observed in the $(R - I)$ CMD of the Pleiades (Bouvier et al 1998), in agreement with the theoretical predictions (Chabrier et al 2000). This clearly illustrates the effect of grain formation in the atmosphere, which affects the spectra of LMS and SSOs below $T_{\rm eff} \lesssim 2400$ K. In the near-infrared color $(J\text{-}K)$ (Figure 13, see color insert), grain condensation yields very red colors for the DUSTY models, whereas COND and grainless models loop back to short wavelengths (blueward) below $m \sim 0.11\,M_\odot$, $M_K \sim 10$ for [M/H] $= -2$, and $m \sim 0.072\,M_\odot$ (resp. $\sim 0.04\,M_\odot$) at 5 Gyr (resp. 100 Myr) for solar metallicity, i.e. $M_K \sim 12$. As described in Section 2.2, this stems from (1) the onset of H_2 CIA for low-metallicity objects and (2) the formation of CH_4 at the expense of CO when the peak of the Planck function moves in the wavelength range characteristic of the absorption bands of this species, for solar-like abundances.

In terms of colors, there is a competing effect between grain and molecular opacity sources for objects at the bottom and just below the MS. The backwarming effect resulting from the large grain opacity destroys molecules such as e.g H_2O, one of the main sources of absorption in the near-IR (cf Section 2.2.1), and yields the severe reddening near the bottom of the MS ($T_{\rm eff} \lesssim 2300$–2400 K), as illustrated by the DENIS (Tinney et al 1998) and 2MASS (Kirkpatrick et al 1999a) objects and by GD165B (Kirkpatrick et al 1999b). As the temperature decreases, grains condense and settle at deeper layers below the photosphere, while methane absorption in the IR increases (see Section 2.2) so that the peak of the flux will move back to shorter wavelengths and the color sequence will go from the DUSTY one to the COND one. The exact temperature at which this occurs is still uncertain because it involves the complex grain thermochemistry and dynamics outlined in Section 2.2, but it should lie between $T_{\rm eff} \sim 1000$ K, for Gl229B, and $\sim$1700 K, corresponding to $J\text{-}K \sim 2$ for the presently reddest observed L-dwarf with known parallax LHS102B (Goldman et al 1999, Basri et al 2000).

In spite of the aforementioned strong absorption in the IR, BDs around 1500 K radiate nearly 90% (99% with dust) of their energy at wavelengths longward of $1\,\mu$m, and infrared colors are still preferred to optical colors (at least for solar metal abundance), with J, Z, H as the favored bands for detection, and $M_M \sim M_{L'} \sim 10$–11, $M_K \sim M_J \sim 11$–12 at the H-burning limit, at 1 Gyr (see Chabrier et al 2000).

4.5.3 Halo Stars. Globular Clusters

Observations of LMS belonging to the stellar halo population of our Galaxy (also called "spheroid" to differentiate it from the $\rho(r) \propto 1/r^2$ dark halo) or to globular clusters down to the bottom of the MS have been rendered possible with the HST optical (WFPC2) and IR (NICMOS) cameras and with parallax surveys at very faint magnitudes (Leggett

1992, Monet et al 1992, Dahn et al 1995). This provides stringent constraints for our understanding of LMS structure and evolution for metal-depleted objects. The reliability of the LMS theory outlined in Section 2 has been assessed by the successful confrontation to various observed sequences of globular clusters ranging from $[M/H] \simeq -2.0$ to -1.0[2] (Baraffe et al 1997). Figure 8 in Baraffe et al (1997) portrays several tracks for different metallicities, corresponding to the MS of various globular clusters. The tracks are superposed with the subdwarf sequence of Monet et al (1992), which is identified as stellar halo objects from their kinematic properties. As shown in this figure, the pronounced variations of the slope in the CMD around $\sim 0.5\,M_\odot$ and $\sim 0.2\,M_\odot$, which stem from the very physical properties of the stars—namely the onset of molecular absorption in the atmosphere and of degeneracy in the core (see Section 2)—are well reproduced by the theory at the correct magnitudes and colors. The predicted blue loop in IR colors caused by the ongoing CIA absorption of H_2 for the lowest-mass (coolest) objects (see Section 2.2.1 and Figure 13 for [M/H] = −2), has also been confirmed by observations with the NICMOS camera (Pulone et al 1998).

4.6 The Lithium and Deuterium Tests

One ironclad certification of a BD is a demonstration that hydrogen fusion has not occurred in its core. As Figure 2 illustrates, lithium burning through the $Li^7(p, \alpha)\,He^4$ reaction occurs at a lower temperature than is required for hydrogen fusion. The timescale for the destruction of lithium in the lowest-mass stars is about 100 Myr. Moreover, the evolutionary timescale in LMS/BDs is many orders of magnitude larger than the convective timescale (see e.g. Bildsten et al 1997), so core abundances and atmospheric abundances can be assumed identical. Therefore, the retention of lithium in a fully mixed object older than 10^8 yr signifies the lack of hydrogen burning. This provides the basis of the so-called "lithium-test" first proposed by Rebolo et al (1992) to identify bona-fide BDs. Evolutionary models based on non-grey atmospheres and the screening factors described in Section 2.1.2 yield a lithium-burning minimum mass $m_{Li} \simeq 0.06\,M_\odot$ (Chabrier et al 1996). Note from Figure 2 the strong age dependence of the lithium test: Young stars at $t \lesssim 10^8$ yr (depending on the mass) will exhibit lithium (which in passing precludes the application of the lithium test for the identification of SSOs in star forming regions), whereas massive BDs within the mass range [0.06–0.07 $M_\odot$] older than $\sim 10^8$ yr will have burned lithium.

By observing a young cluster older than $\sim 10^8$ yr, one can look for the boundary-luminosity below which lithium has not yet been depleted. Objects fainter than

---

[2]Globular clusters with an observed $[Fe/H]$ must be compared with theoretical models with the corresponding metallicity $[M/H]$ = [Fe/H] + [O/Fe] in order to take into account the enrichment of α-elements (see Baraffe et al 1997).

this limit will definitely be in the substellar domain. Conversely, the determination of the lithium depletion edge yields the age of the cluster, as was first proposed by Basri et al (1996) (see also e.g. Stauffer et al 1998). Indeed, the lithium test provides a "nuclear" age that may be even more powerful a diagnostic than the conventional nuclear age from the upper main sequence turn-off, since the evolution of the present fully convective low-mass objects does not depend on ill-constrained parameters such as mixing length or overshooting. As noted by Stauffer et al (1998), the age-scale for open clusters based on the (more reliable) lithium depletion boundary has important implications for stellar evolution: The ages of several clusters (Pleiades, α-Per, IC 2391) are all consistent with a small but non-zero amount of overshooting to be included in the evolutionary models at the turn-off mass in order to yield similar ages. See Basri (this issue) for a more detailed discussion of the lithium test. The deuterium-test can be used in a similar manner, extending the lithium test to smaller masses and younger ages, typically t $\lesssim 10^7$ yr (Béjar et al 1999). The D-burning minimum mass is predicted as $m_D \simeq 0.013\,M_\odot$ (see Figure 2) and has been proposed (Shu et al 1987) as playing a key role in the formation of isolated star-like objects, in contrast to objects formed in a protoplanetary disk. Deuterium-depletion is illustrated in Figure 14 (see color insert). This figure displays the evolution of SSOs above m_D in the I-band. The left and right diagonal solid lines correspond to 50% D-depletion ($[D]/[D]_0 = 1/2$) and 99% D-depletion, respectively ($[D]_0 = 2 \times 10^{-5}$ is the initial mass fraction). The inset displays the corresponding curves in $T_{\rm eff}$. Spectroscopic signatures of deuterium include absorption lines of deuterated water HDO between 1.2 and 2.1 μm (Toth 1997). The observation of deuterated methane CH_3D cannot be used for the deuterium test as an age-indicator; at the temperature methane forms ($\lesssim$1800 K), SSOs above the D-burning minimum mass are old enough for all deuterium to have been burned (see Figure 6).

4.7 Low-Mass Objects in Cataclysmic Variables

The study of cataclysmic variables (CVs) is closely related to the theory of LMS and SSOs regarding their inner structure and the magnetic field generation. CVs are semi-detached binaries with a white dwarf (WD) primary and a low-mass stellar or substellar companion ($m \lesssim 1\,M_\odot$) that transfers mass to the WD through Roche-lobe overflow (see e.g. King 1988 for a review). In the current standard model, mass transfer is driven by angular momentum loss caused by magnetic wind braking for predominantly radiative stars, and by gravitational wave emission for fully convective objects. The Roche lobe filling the secondary's mean density $\bar\rho$ determines almost entirely the orbital period P, with $P_h = k/\bar\rho^{1/2}$ (where $k \simeq 8.85$ is a weak function of the mass ratio, P_h is the orbital period in hr, and $\bar\rho = (m_2/R_2^3)/(M_\odot/R_\odot^3)$ is the mean density of the secondary in solar units) (see King 1988). For objects obeying classical mechanics, i.e. in the stellar regime, $m \propto R$ (see Section 3.1 and Figure 3) so that the mean density increases with

decreasing mass ($\bar{\rho} \propto 1/m^2$) and the orbital period decreases along evolution as the secondary loses mass $P_h \propto 1/\bar{\rho}^{1/2} \propto m_2$. The situation reverses near and below the HBMM when electron degeneracy dominates. In that case, the radius increases very slightly with decreasing mass (Figure 3), so that the mean density is essentially proportional to the mass ($\bar{\rho} \propto m$) and the orbital period increases along evolution $P_h \propto \sim m_2^{-1/2}$. Then the secular evolution of the orbital period reverses when the donor becomes a BD. The analysis of CV orbital evolution thus provides important constraints on LMS and BD internal structure.

The major puzzle of CVs is the observed distribution of orbital periods, namely the dearth of systems in the 2–3 h period range and the minimum period P_{min} at 80 min (see King 1988). The most popular explanation for the period gap is the disrupted magnetic braking scenario (Rappaport et al 1983, Spruit & Ritter 1983), and most evolutionary models including this process do reproduce the observed period distribution. However, the recent progress realized in the field of LMS and SSOs now allows the confrontation of the theoretical predictions with the observed atmospheric properties (colors, spectral types) of the secondaries (Beuermann et al 1998, Clemens et al 1998, Kolb & Baraffe 1999a). The aforementioned standard period-gap model may be in conflict with the observed spectral type of some CV secondaries (Beuermann et al 1998, Kolb & Baraffe 1999b). Although alternative explanations exist for the period gap, none of them has been proven as successful as the disrupted magnetic braking scenario. The most recent alternative suggestion, based on a characteristic feature of the mass-radius relationship of LMS (Clemens et al 1998), has been shown to fail to reproduce the observed period distribution around the period gap (Kolb et al 1998). On the other hand, as we discussed in Section 2.3, no change in the level of activity is observed in isolated M-dwarfs along the transition between partially and fully convective structures at $m \sim 0.35\, M_\odot$ and $Sp \sim$ M2–M4, which indicates that a magnetic field is still generated in the mass-range corresponding to the CV gap. In this case, the abrupt decrease of angular momentum losses by magnetic braking at the upper edge of the period gap could result from a rearrangement of the magnetic field when stars become fully convective, without necessarily implying a sudden decline in the magnetic activity, as suggested by Taam & Spruit (1989; see also Spruit 1994).

Finally, an $\sim$10% discrepancy still remains between the theoretical and the observed minimum period $P_{min} = 80$ min, even when we include the most recent improvements in stellar physics (see Kolb & Baraffe 1999a for details). Residual shortcomings in the theory, either in the EOS or in the atmosphere, cannot be ruled out as the cause of this discrepancy. Alternatively, an additional driving mechanism to gravitational radiation in fully convective objects can reconcile predicted and observed P_{min} (Kolb & Baraffe 1999a). Because magnetic activity is still observed in fully convective, late spectral type, M-dwarfs, magnetic braking could operate in CV secondaries even down to P_{min}, but with a weaker efficiency than above the period gap. These open questions certainly require a better understanding of

magnetic field generation and dissipation in LMS and BDs, a point already stressed in Section 2.3.

5. GALACTIC IMPLICATIONS

5.1 Stellar Luminosity Function and Mass Function

It is now well established that visible stars are not numerous enough to account for the dynamics of our Galaxy—the so-called galactic dark-matter problem. A precise determination of their density requires the correct knowledge of the luminosity function (LF) down to the H-burning limit, and a correct transformation into a mass-function (MF). The latter issue has been improved significantly with models that describe more accurately the color-color and color-magnitude diagrams of LMS and BDs for various metallicities, and most importantly, that provide mass-magnitude relationships in good agreement with the observations (see Section 4). The former issue, however, is not completely settled at present, and significant differences still exist among various determinations of the nearby LF and between the nearby LF and the photometric LF determined from the ground and with the HST, as shown later in this section.

The main problem with the nearby sample is the limited number of stars at faint magnitudes. Although the sample is complete to 20 pc for stars with $M_V < 9.5$, it is severely incomplete beyond 5 pc for $M_V > 12$ (Henry et al 1997). Kroupa (unpublished) derived a nearby LF Φ_{near} by combining Hipparcos parallax data (which is essentially complete for $M_V < 12$ at r = 10 pc) and the sample of nearby stars (Dahn et al 1986) with ground-based parallaxes for $V > 12$ to a completeness distance r = 5.2 pc. The nearby LF determined by Reid & Gizis (1997) is based on a volume sample within 8 pc. Most of the stars in this survey have parallaxes. For all the late K and M dwarfs, however, trigonometric parallaxes are not available, and these authors use a spectroscopic TiO-index vs M_V^{TiO} relation to estimate the distance (Reid et al 1995). This sample was revised recently with Hipparcos measurements and new binary detections in the solar neighborhood (Delfosse et al 1999a) and leads to a revised northern 8-pc catalogue and nearby LF (Reid et al 1999). These authors argue that their sample should be essentially complete for $M_V < 14$. However, the analysis of completeness limits by Henry et al (1997, their Figure 1) shows that the known stellar census becomes substantially incomplete for distances larger than 5 pc. About 35% of the systems in the Reid et al sample are multiple, and ∼45% of all stars have a companion in binary or multiple systems.

The photometric LFs, Φ_{phot}, based on large observed volumes via deep pencil-beam surveys, avoid the limitation because of small statistics but introduce other problems such as Malmquist bias and unresolved binaries (see e.g. Kroupa et al 1993, Kroupa 1995), yielding only the determination of the stellar *system* LF. For the HST LF (Gould et al 1997), with $I \lesssim 24$, the Malmquist bias is negligible
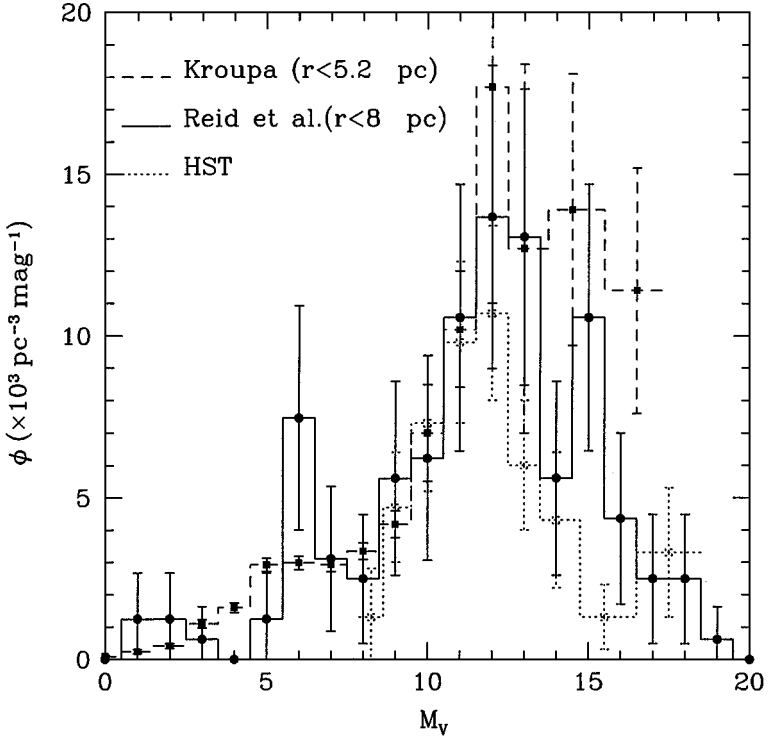
Figure 15   Luminosity function in the V-band from the 5-pc sample (*dashed-line*) (Kroupa, unpublished), the 8-pc sample (*solid-line*) (Reid et al 1999) and from the HST (*dotted-line*) (Gould et al 1998).

because all stars down to $\sim 0.1\,M_\odot$ are seen through to the edge of the thick disk. A major caveat of photometric LFs, however, is that the determination of the distance relies on a photometric determination from a color-magnitude diagram. In principle this requires the determination of the metallicity of the stars, since colors depend on metallicity (see Figure 12, see color insert). The illustration of the disagreement among the three aforementioned LFs, Φ_{5pc}, Φ_{8pc}, and Φ_{HST}, at faint magnitude is apparent in Figure 15. The disagreement between the two nearby LFs, in particular, presently has no robust explanation. It might come from incompleteness of the 8 pc sample at faint magnitudes. Note also that in the spectroscopic relation used to estimate the distance, M_V can be uncertain by ~ 1 mag (see Figure 3 of Reid et al 1995), certainly a source of Malmquist bias, even though the number of stars without parallax in this sample is small ($\sim 10\%$) and a Malmquist bias on this part should not drastically affect the results. On the other hand, as noted in Section 4.1, the end of the 5-pc sample might be contaminated by a statistically significant number of young BDs, or by stars with slightly under-solar abundances.
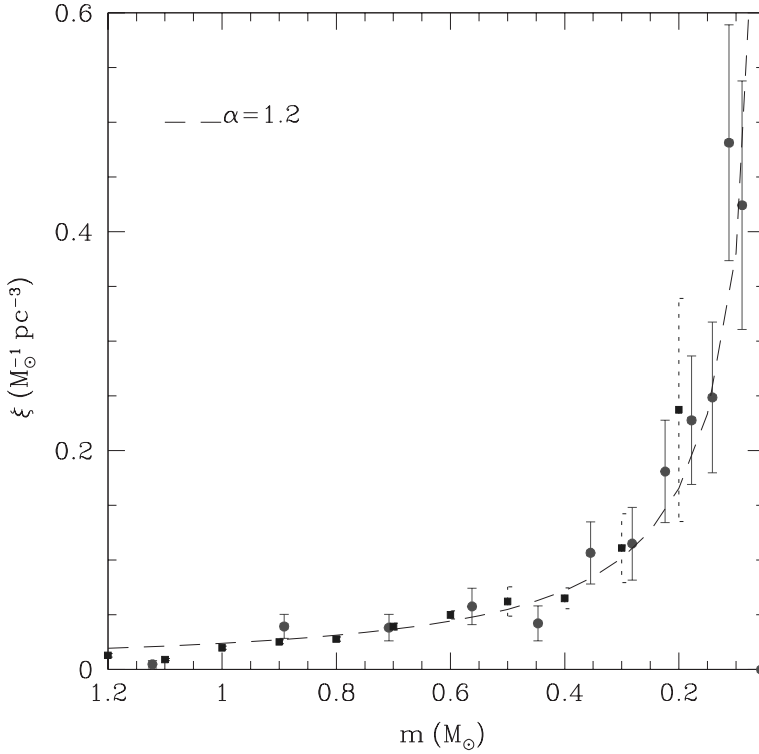
Figure 16   Mass function derived from the 5-pc LF (*squares*, last bin out of the figure) and the 8-pc LF (*circles*). *Dashed-line*: $dn/dm = 0.024\,m^{-1.2}$ (see text).

Figure 16 compares the MFs obtained from the two aforementioned nearby LFs, using the mass-magnitude relations described in Section 4.2. In practice, the observed sample constitutes a mixture of ages and metallicities. However, the Hipparcos CMD indicates that $\sim$90% of disk stars have $-0.3 < [M/H] < 0.1$ (Reid 1999), so the spread of metallicity is unlikely to significantly affect the derivation of the MF through the mass-magnitude relation. Moreover, the choice of m-M_K minimizes metallicity effects; see Figure 9, also Figure 3 of Baraffe et al 1998. The MS lifetimes for stars with m $\lesssim 1\,M_\odot$ are longer than a Hubble time, and age variations in the mass-magnitude relation will affect only objects $\lesssim 0.15\,M_\odot$ younger than $\sim$0.5 Gyr (see Figure 9).

Superposed is a power-law MF normalized at $0.8\,M_\odot$ on the Hipparcos sample $dn/dm = 0.031(m/0.8)^{-\alpha} = 0.024\,m^{-\alpha}\,M_\odot^{-1}pc^{-3}$ with $\alpha = 1.2$. As shown in the Figure 16, this provides a very reasonable description of the low-mass part of the MF, within a variation of $\sim$10% for α, thus confirming the previous analysis of Kroupa et al (1993)—except for the very last bin obtained from Kroupa's LF,

which predicts about twice as many stars at 0.1 $M_\odot$ (out of the figure). Similar results are obtained from the bolometric and M_K-LFs for the 8-pc sample. Integration of this MF yields very-low-mass stars ($m \leq 0.8\,M_\odot$), number- and mass-densities $n_{VLMS} \simeq 7.0 \times 10^{-2}$ pc^{-3} and $\rho_{VLMS} \approx 2.0 \times 10^{-2}$ M$_\odot$pc^{-3}, respectively. Adding up the contribution from more massive stars, $\rho_{>0.8} \approx 1.4 \times 10^{-2}$ M$_\odot$pc^{-3} (Miller & Scalo 1978) and stellar remnants, $\rho_{WD+NS} \approx 3.0 \times 10^{-3}$ M$_\odot$pc^{-3} yields a stellar density $\rho_\star \approx 3.4 \times 10^{-2}$ M$_\odot$pc^{-3} in the Galactic disk, i.e. a surface density $\sum_\star \approx 22 \pm 2$ M$_\odot$pc^{-2} (assuming a scale height $h = 320$ pc). A Salpeter MF, $dn/dm \propto m^{-2.35}$, all the way down to the bottom of the MS would overestimate the density at 0.1 $M_\odot$ by more than a factor of 10.

For the Galactic spheroid, the question is more settled. The LFs determined from nearby surveys (Dahn et al 1995) and from the HST (Gould et al 1998) are comparable within about 2 sigmas, and yield a MF with $\alpha \lesssim 1$ (Graff & Freese 1996, Chabrier & Méra 1997, Gould et al 1998) and a stellar number-and mass-density $n_\star < 10^{-3}\ pc^{-3}$ and $\rho_\star < 4.0 \times 10^{-5}$ M$_\odot$pc^{-3}, i.e. an optical depth $\tau \sim 10^{-9}$, about 1% of the value measured toward the LMC. At present the dark halo MF is completely unknown, but both the Hubble Deep Field observations and the narrow-range of the observed time-distribution of the microlensing events toward the LMC strongly suggest an IMF different from a Salpeter IMF below $\sim$1 $M_\odot$ (Chabrier 1999). Assuming a homogeneous distribution, both constraints yield a mass-density for LMS in the dark halo about two orders of magnitude smaller than the afore-mentioned spheroid one (Chabrier & Méra 1997). This means that essentially no stars formed below about a solar mass in the dark halo.

5.2   Brown Dwarf Mass Function

Even though the possibility that BDs could make up for the Galactic missing mass is now clearly excluded, a proper census of the number of BDs has significant implications for our understanding of how stars and planets form. The determination of the BD MF is a complicated task. By definition, BDs never reach thermal equilibrium, and most of the BDs formed at the early stages of the Galaxy will have dimmed to very low luminosities ($L \propto 1/t$). Thus, observations will be biased toward young and massive BDs. This age-undetermination is circumvented when we study the BD MF in clusters because objects in this case are likely to be coeval. The Pleiades cluster has been extensively surveyed, and several BDs have been identified down to $\sim$0.04 $M_\odot$ (Martín et al 1998, Bouvier et al 1998, Hambly et al 1999). A single power-law function from $\sim$0.4 to 0.04 $M_\odot$ seems to adequately reproduce the observations (not corrected for binaries) with some remaining uncertainties in the exponent: $\alpha \sim$ 0.6–1.0. However, stellar objects in very young clusters ($\lesssim 10^6$ yr) might still be accreting, whereas older clusters may have already experienced significant dynamical evolution, mass segregation in the core, and/or evaporation in the outer regions (see e.g. Raboud & Mermilliod 1998). In this case, the present-day mass function does not reflect the initial mass function. For

these reasons, it is probably premature to claim a robust determination of the MF in young clusters.

The DENIS (Delfosse et al 1999b) and 2MASS (Kirkpatrick et al 1999b, Burgasser et al 1999) surveys, which have covered an area of several hundred square degrees and are complete to $K = 13.5$ and 14.5 respectively, have revealed about 20 field L-dwarfs and 4 field methane-BDs. This yields an L-dwarf number-density $n_L \approx 0.03 \pm 0.01$ sq deg^{-1} for $K < 14.5$ and a methane-BD number-density $n_{CH_4} \approx 0.002$ sq deg^{-1} for $J < 16$. Although these numbers correspond to small statistics and should be considered with caution, they provide the first observational constraints on the substellar MF in the Galactic disk and are consistent with a slowly rising BD MF with $\alpha \simeq 1-2$ (Reid et al 1999; Chabrier, in preparation), assuming a constant formation rate.

Independent, complementary information on the stellar and substellar MF comes from microlensing observations. Indeed, the time distribution of the events provides a (model-dependent) determination of the mass-distribution and thus of the minimum mass of the dark objects: $dN_{ev}/dt_e = E \times \epsilon(t_e) \times d\Gamma/dt_e \propto P(m)/\sqrt{m}$, where E is the observed exposure (i.e. the number of star $\times$ years), ϵ is the experimental efficiency, Γ is the event rate, and $P(m)$ is the mass probability distribution. The analysis of the published 40 MACHO (Alcock et al 1997) + 9 OGLE (Udalsky et al 1994) events toward the bulge is consistent with a rising MF at the bottom of the MS, whereas a decreasing MF below 0.2 $M_\odot$ seems to be excluded at a high (>90%) confidence level (Han & Gould 1996, Méra et al 1998). Although the time distribution might be affected by various biases (e.g. blending) and robust conclusions must wait for larger statistics, the present results suggest that, in order to explain both star counts and the microlensing experiments, a substantial number of BDs must be present in the Galactic disk. Extrapolation of the stellar MF determined in Section 5.1 into the BD domain down to 0.01 $M_\odot$ yields for the Galactic disk a BD (*number*) density comparable to the stellar one, $n_{BD} \approx 0.1 \, pc^{-3} \simeq n_\star$, and a mass-density $\rho_{BD} \approx 3.0 \times 10^{-3}$ M$_\odot$pc^{-3}, i.e. $\sum_{BD} \approx 2$ M$_\odot$pc^{-2}.

For the spheroid, extrapolation of the previously determined stellar MF yields $n_{BD} \lesssim 10^{-3} \, pc^{-3}$, $\rho_{BD} \lesssim 10^{-5}$ M$_\odot$pc^{-3}, less than 0.1% of the required dynamical density. For the dark halo the density is about two orders of magnitude smaller, as mentioned before.

It is obviously premature to try to infer the mass distribution of exoplanets. This will first require a clear theoretical and observational distinction between planets and brown dwarfs. However, an interesting preliminary result comes from the observed mass distribution of the companions of G and K stars. As shown in Figure 4 of Mayor et al (1998), there is a strong discontinuity in the mass distribution at $m_2/\sin i \approx 5 \, M_J$, with a clear peak below this limit. This suggests that planet formation in a protoplanetary disk is a much more efficient mechanism than BD formation as star companions, at least around G and K stars (see e.g. Marcy & Butler 1998). It also suggests that the MF for BD stellar companions

differs from the MF in the field. Ongoing observations around M-stars will tell us whether such a mass distribution still holds around low-mass stars.

6. CONCLUSIONS

This review has summarized the significant progress achieved within the past few years in the theory of cool and dense objects at the bottom of and beyond the main sequence: low-mass stars, brown dwarfs, and gaseous planets. The successful confrontation of the theory with the numerous detections of low-mass stellar and substellar objects allows a better understanding of their structural and thermal properties, and allows reliable predictions about their evolution. This in turn brings confidence in the predicted characteristic properties of these objects, a major issue in terms of search strategies for future surveys.

Important problems remain to be solved to improve the theory. A non-exhaustive list includes, for example: (1) a better determination of the EOS in the pressure-ionization region, with the possibility of a first-order phase transition; (2) the study of phase separation of elements in SSO interiors; (3) an improved treatment of convection in optically-thin regions; (4) a precise description of the dynamics of grain formation and sedimentation in SSO atmospheres; (5) the derivation of an accurate mass-T_{eff}-age scale for SSOs and young objects; and (6) a correct understanding of magnetic-field generation and dissipation in active LMS and BDs.

The increasing number of observed LMS and SSOs, together with the derivation of accurate models, eventually will allow a robust determination of the stellar and substellar mass functions, of the minimum mass for the formation of star-like objects, and thus of the exact density of these objects in the Galaxy. As we discussed in Section 5, present determinations in various Galactic regions point to a slowly rising MF near and below the H-burning limit, with a BD number-density comparable to the stellar one and an MF truncated below $\sim$1 $M_\odot$ in the dark halo. A more precise determination must await confirmation from future observations. At last, the amazingly rapid pace of exoplanet discoveries should yield the determination of the planetary MF and maximum mass, and eventually the direct detection of such objects, a future formidable test for the theory.

Visit the Annual Reviews home page at www.AnnualReviews.org

LITERATURE CITED

Alcock C, Allsman RA, Alves D, Axelrod TS, Bennett DP, et al. 1997. *Ap. J.* 479: 119

Alexander DR, Ferguson JW. 1994. *Ap. J.* 437:879

Allard F. 1990. PhD thesis. Univ. Heidelberg, Germany. 160 pp.

Allard, F. 1999. *Proc. Euroconference, La Palma*

Allard F, Alexander DR, Tamanai A, Hauschildt P. 1998. *Proc. ASP Conf. Series* 134:438

Allard F, Hauschildt PH. 1995. *Ap. J.* 445:433

Allard F, Hauschildt PH, Alexander DR, Starrfield S. 1997. *Annu. Rev. Astron. Astrophys.* 35:137

Allard F, Hauschildt PH, Alexander DR, Tamanai A, Ferguson J. 2000. *Ap. J.* In press

Allard F, Hauschildt PH, Baraffe I, Chabrier G. 1996. *Ap. J.* 465:L123

Auman J. 1969. *Low Luminosity Stars.* New York: Gordon and Breach, 539 pp.

Baraffe I, Chabrier G. 1996. *Ap. J.* 461:L51

Baraffe I, Chabrier G, Allard F, Hauschildt PH. 1995. *Ap. J.* 446:L35

Baraffe I, Chabrier G, Allard F, Hauschildt PH. 1997. *Astron. Astrophys.* 327:1054

Baraffe I, Chabrier G, Allard F, Hauschildt PH. 1998. *Astron. Astrophys.* 337:403

Basri G, Marcy GW, Graham JR. 1996. *Ap. J.* 458:600

Basri G, Mohanty S, Allard F, Hauschildt PH, Delfosse X, et al. 2000. *Ap. J.* In press

Béjar VJS, Zapatero Osorio MR, Rebolo R. 1999. *Ap. J.* 521:671

Beuermann K, Baraffe I, Kolb U, Weichhold M. 1998. *Astron. Astrophys.* 339:518

Bildsten L, Brown EF, Matzner CD, Ushomirsky G. 1997. *Ap. J.* 482:442

Borysow A, Jorgensen UG, Zheng C. 1997. *Astron. Astrophys.* 324:185

Bouvier J, Stauffer JR, Martín EL, Barrado y Navascues B, Wallace B, Béjar VJS. 1998. *Astron. Astrophys.* 336:490

Brett C. 1995. *Astron. Astrophys.* 295:736

Brett C, Plez B. 1993. *Astron. Soc. Aust. Proc.* 10:250

Burgasser AJ, Kirkpatrick JD, Brown NE, Reid IN, et al. 1999. *Ap. J.* 522:65

Burrows A, Hubbard WB, Lunine JI. 1989. *Ap. J.* 345:939

Burrows A, Hubbard WB, Saumon D, Lunine JI. 1993. *Ap. J.* 406:158

Burrows A, Hubbard WB, Lunine JI. 1994. *Cool Stars, Stellar Systems and the Sun. ASP.* 64:528

Burrows A, Liebert J. 1993. *Rev. Mod. Phys.* 65:301

Burrows A, Marley M, Hubbard WB, Lunine JI, Guillot T, et al. 1997. *Ap. J.* 491:856

Burrows A, Marley M, Sharp CM. 2000. *Ap. J.* 531:43

Burrows A, Sharp CM. 1999. *Ap. J.* 512:843

Canuto VM, Goldman I, Mazzitelli I. 1996. *Ap. J.* 473:550

Canuto VM, Mazzitelli I. 1991. *Ap. J.* 370: 295

Caughlan GR, Fowler WA. 1988. *Atom. Data Nucl. Data Tables* 40:283

Chabrier G. 1990. *J. Phys.* 51:1607

Chabrier G. 1999. *Ap. J.* 513:L103

Chabrier G, Baraffe I. 1997. *Astron. Astrophys.* 327:1039

Chabrier G, Baraffe I, Allard F, Hauschildt PH. 2000. *Ap. J.* In press

Chabrier G, Baraffe I, Plez B. 1996. *Ap. J.* 459:L91

Chabrier G, Méra D. 1997. *Astron. Astrophys.* 328:83

Clausen JV, Helt BE, Olsen EH. 1999. *Theory and tests of convection in stellar structure.* ASP Conf. Series 173, *Am. Soc. Phys.*

Clayton DD. 1968. *Principles of Stellar Evolution and Nucleosynthesis.* Chicago: Chicago Press, 612 pp.

Clemens JC, Reid IN, Gizis JE, O'Brien MS. 1998. *Ap. J.* 496:392

Collins GW, Da Silva LB, Celliers P, Gold DM, Foord ME, et al. 1998. *Science* 281: 1178

Copeland H, Jensen JO, Jorgensen HE. 1970. *Astron. Astrophys.* 5:12

Cox JP, Guili RT. 1968. *Principles of Stellar Structure.* New York: Gordon and Breach 1305 pp.

Dahn CC, Guetter HH, Harris HC, Henden AA, Luginbuhl CB, et al. 1999. The evolution of galaxies on cosmological timescales. *ASP Conf. Series*

Dahn CC, Liebert J, Harris HC, Guetter HH. 1995. The bottom of the main sequence and beyond. *ESO Astrophys. Symp.*, p. 239. Berlin/Heidelberg: Springer Verlag

Dahn CC, Liebert J, Harrington RS. 1986. *Astron. J.* 91:621

Da Silva, et al. 1997. *Phys. Rev. Lett.* 78:483

D'Antona F, Mazzitelli I. 1985. *Ap. J.* 296:502

Delfosse X, Forveille T, Beuzit JL, Udry S, Mayor M, Perrier C. 1999a. *Astron. Astrophys.* 344:897

Delfosse X, Forveille T, Perrier C, Mayor M. 1998a. *Astron. Astrophys.* 331:581

Delfosse X, Forveille T, Tinney CG, Epchtein N. 1998b. See Allard et al. 1998, p. 67

Delfosse X, Tinney CG, Forveille T, Epchtein N, Bertin E, et al. 1997. *Astron. Astrophys.* 327:L25

Delfosse X, Tinney CG, Forveille T, Epchtein N, Borsenberger J, et al. 1999b. *Astron. Astrophys. Suppl.* 135:41

Delfosse X, Forveille T, Udry S, Beuzit JL, Mayor M, Perrier C. 1999c. *Astron. Astrophys. Lett.* 350:L39

Demarque P, Guenther DB, Kim Y-C. 1999. *Ap. J.* 517:510

Dorman B, Nelson LA, Chau WY. 1989. *Ap. J.* 342:1003

Durney B, De Young DS, Roxburgh IW. 1993. *Solar Phys.* 145:207

Fegley B, Lodders K. 1994. *Icarus* 110:117

Fegley B, Lodders K. 1996. *Ap. J.* 472:L37

Fontaine G, Graboske HC, VanHorn HM. 1977. *Ap. J. Suppl.* 35:293

Forveille T, Beuzit JL, Delfosse X, Segransan D, Beck F, et al. 1999. *Astron. Astrophys.* 351:619

Goldman B, Delfosse X, Forveille T, Afonso C, Alard C, et al. 1999. *Astron. Astrophys.* 351:L5

Gould A, Flynn C, Bahcall JN. 1998. *Ap. J.* 503:798

Gould A, Bahcall JN, Flynn C. 1997. *Ap. J.* 482:913

Graff D, Freese K. 1996. *Ap. J.* 456:49

Griffith CA, Yelle RV, Marley MS. 1998. *Science* 282:2063

Grossman AS, Hays D, Graboske HC. 1974. *Astron. Astrophys.* 30:95

Grossman L. 1972. *Geochim. Cosmochim. Acta* 36:597

Guillot T. 1995. *Science* 269:1697

Guillot T. 1999. *Science* 286:72

Guillot T, Burrows A, Hubbard WB, Lunine JI, Saumon D. 1996. *Ap. J.* 459:L35

Hambly NC, Hodgkin ST, Cossburn MR, Jameson RF. 1999. *MNRAS* 303:835

Han C, Gould A. 1996. *Ap. J.* 467:540

Hauschildt PH, Allard F, Baron E. 1999. *Ap. J.* 512:377

Hawley SL, Gizis JE, Reid IN. 1996. *Astron. J.* 112:2799

Henry TJ, McCarthy DW. 1993. *Astron. J.* 106:773

Henry TJ, Ianna PA, Kirkpatrick D, Jahreiss H. 1997. *Astron. J.* 114:388

Hubbard WB. 1977. *Icarus* 30:305

Hubbard WB. 1994. The equation of state in astrophysics. *Proc. IAU Coll., Saint-Malo, 1993.* 147:443. Cambridge, UK: Cambridge University Press

Hümmer DG, Mihalas D. 1988. *Ap. J.* 331:794

Iglesias CA, Rogers FJ. 1996. *Ap. J.* 464:943

Jones HRA, Tsuji T. 1997. *Ap J.* 480:L39

Kirkpatrick JD, Allard F, Bida T, Zuckerman B, Becklin EE, et al. 1999b. *Ap. J.* 519:834

Kirkpatrick JD, Henry TJ, McCarthy DW. 1991. *Ap. J. Suppl.* 77:417

Kirkpatrick JD, McCarthy DW. 1994. *AJ.* 107:333

Kirkpatrick JD, Reid IN, Liebert J, Cutri RM, Nelson B, et al. 1999a. *Ap. J.* 519:802

King AR. 1988. *Q. J. R. Astron. Soc.* 29:1

Kolb U, Baraffe I. 1999a. *MNRAS* 309:1034

Kolb U, Baraffe I. 1999b. Annapolis workshop on magnetic cataclysmic variables. *ASP Conf. Series.* 197:273

Kolb U, King AR, Ritter H. 1998. *MNRAS* 298:L29

Kroupa P. 1995. *Ap. J.* 453:350

Kroupa P, Tout CA, Gilmore G. 1990. *MNRAS* 244:76

Kroupa P, Tout CA, Gilmore G. 1993. *MNRAS* 262:545

Kumar SS. 1963. *Ap. J.* 137:1121

Leggett S. 1992. *Ap. J. Suppl.* 82:351

Leggett S, Allard F, Berriman G, Dahn CC, Hauschildt PH. 1996. *Ap. J. Suppl.* 104:117

Leggett S, Allard F, Hauschildt PH. 1998. *Ap. J.* 509:836

Lenzuni P, Chernoff DF, Salpeter EE. 1991. *Ap. J. Suppl.* 76:759

Leung KC, Schneider D. 1978. *Astron. J.* 83:618

Linsky J. 1969. *Ap. J.* 156:989

Lodders K. 1999. *Ap. J.* 519:793

Ludwig HG, Freytag B, Steffen M. 1999. *Astron. Astrophys.* 346:111

Luhman KL. 1999. *Ap. J.* 525:466

Lunine JI, Hubbard WB, Burrows A, Wang YP, Garlow K. 1989. *Ap. J.* 338:314

Lunine JI, Hubbard WB, Marley MS. 1986. *Ap. J.* 310:238

Magni G, Mazzitelli I. 1979. *Astron. Astrophys.* 72:134

Marcy GW, Butler RP. 1998. *Annu. Rev. Astron. Astrophys.* 36:57

Marley MS, Gelino C, Stephens D, Lunine JI, Freedman R. 1999. *Ap. J.* 513:879

Marley MS, Hubbard WB. 1988. *Icarus* 73:536

Marley MS, Saumon D, Guillot T, Freedman RS, Hubbard WB, et al. 1996. *Science* 272:1919

Martín E. 1999. See Allard 1999

Martín EL, Basri G, Delfosse X, Forveille T. 1997. *Astron. Astrophys.* 327:L29

Martín EL, Basri G, Zapatero-Osorio MR, Rebolo R, Lopez RJ. 1998. *Ap. J.* 507: L41

Maxted PFL, Marsh TR, Moran C, Dhillon VS, Hilditch RW. 1998. *MNRAS* 300:1225

Mayor M, Queloz D. 1995. *Nature* 378:355

Mayor M, Queloz D, Udry S. 1998. See Allard et al. 1998, p. 140

Méra D, Chabrier G, Schaeffer R. 1998. *Astron. Astrophys.* 330:937

Metcalfe TS, Mathieu RT, Latham DW, Torres G. 1996. *Ap. J.* 456:356

Meyer F, Meyer-Hofmeister E. 1999. *Astron. Astrophys.* 341:L23

Miller G, Scalo J. 1978. *PASP.* 90:506

Monet D, Dahn CC, Vrba FJ, Harris HC, Pier JR, et al. 1992. *Astron. J.* 103:638

Nelson LA, Rappaport S, Joss PC. 1986. *Ap. J.* 311:226

Nelson LA, Rappaport S, Chiang E. 1993b. *Ap. J.* 413:364

Nelson LA, Rappaport S, Joss PC. 1993a. *Ap. J.* 404:723

Neuhäuser R, Briceno C, Comeron F, Hearty T, Martín EL, et al. 1999. *Astron. Astrophys.* 343:883

Neuhäuser R, Comeron F. 1998. *Science* 282:83

Noll KS, Geballe TR, Marley MS, 1997. *Ap. J.* 489:L87

Nordlund AA, Stein RF. 1999. See Clausen, et al. 1999, p. 91

Oppenheimer BR, Kulkarni SR, Matthews K, Nakajima T. 1995. *Science* 270:1478

Oppenheimer BR, Kulkarni SR, Matthews K, van Kerkwijk MH. 1998, *Ap. J.* 502:932

Parker EN. 1955. *Ap. J.* 122:293

Parker EN. 1975. *Ap. J.* 198:205

Pulone L, De Marchi G, Paresce F, Allard F. 1998. *Ap. J.* 492:L41

Raboud D, Mermilliod JC. 1998. *Astron. Astrophys.* 333:897

Randich S. 1999. See Allard 1999

Rappaport S, Verbunt F, Joss PC. 1983. *Ap. J.* 275:713

Rebolo R, Martín EL, Magazzù A. 1992. *Ap. J.* 389:L83

Rebolo R, Zapatero Osorio MR, Martín EL. 1995. *Nature* 377:129

Reid IN. 1999. *Annu. Rev. Astron. Astrophys.* 37:191

Reid IN, Gizis JE. 1997. *Astron. J.* 113:2246

Reid IN, Hawley SL, Gizis JE. 1995. *Astron. J.* 110:1838

Reid IN, Kirkpatrick JD, Liebert J, Burrows A, Gizis JE, et al. 1999. *Ap. J.* 521:613

Rossow WB. 1978. *Icarus* 36:1

Ruiz MT, Leggett SK, Allard F. 1997. *Ap. J.* 491:L107

Salpeter EE. 1954. *Aust. J. Phys.* 7:373

Salpeter EE. 1961. *Ap. J.* 134:669

Saumon D. 1994. See Hubbard 1994, p. 306

Saumon D, Bergeron P, Lunine JI, Hubbard WB, Burrows A. 1994. *Ap. J.* 424:333

Saumon D, Chabrier G. 1991. *Phys. Rev. A.* 44:5122

Saumon D, Chabrier G. 1992. *Phys. Rev. A.* 46:2084

Saumon D, Chabrier G, VanHorn HM. 1995. *Ap. J. Suppl.* 99:713

Saumon D, Hubbard WB, Burrows A, Guillot T, Lunine JI, Chabrier G. 1996. *Ap. J.* 460:993

Schatzman E. 1948. *J. Phys. Rad.* 9:46

Schultz AB, Allard F, Clampin M, McGrath M, Bruhweiler FC, et al. 1998. *Ap. J.* 492: L181

Seager S, Sasselov DD. 1998. *Ap. J.* 502: L157

Sharp CM, Huebner WF. 1990. *Ap. J. Suppl.* 72:417

Shu FH, Adams FC, Lizano S. 1987. *Annu. Rev. Astron. Astrophys.* 25:23

Spiegel EA, Weiss NO. 1980. *Nature* 287:616

Spiegel EA, Zahn J-P. 1992 *Astron. Astrophys.* 265:106

Spruit H. 1994. Cosmical magnetism. *NATO ASI Series C.* 422:33–44

Spruit H, Nordlund AA. 1990. *Annu. Rev. Astron. Astrophys.* 28:263

Spruit H, Ritter H. 1983. *Astron. Astrophys.* 124:267

Stauffer JR, Hartmann LW, Prosser CF, Randich S, Balachandran S, et al. 1997. *Ap. J.* 479: 776

Stauffer JR, Schultz G, Kirkpatrick JD. 1998. *Ap. J.* 499:L199

Stein RF, Nordlund. 2000. *Solar Phys.* 192:91

Stevenson DJ. 1979. *Geophys. Astrophys. Fluid Dyn.* 12:139

Stevenson DJ. 1991. *Annu. Rev. Astron. Astrophys.* 29:163

Taam RE, Spruit HC. 1989. *Ap. J.* 345:972

Tarter J. 1975. PhD thesis. Univ. Calif., Berkeley. 120 pp.

Tinney CG, Delfosse X, Forveille T, Allard F. 1998. *Astron. Astrophys.* 338:1066

Tinney CG, Reid IN. 1998. *MNRAS* 301:1031

Toth RA. 1997. *J. Mol. Spect.* 186:276

Tsuji T, Ohnaka K, Aoki W. 1995. See Dahn et al. 1995, p. 45

Tsuji T, Ohnaka K, Aoki W. 1996. *Astron. Astrophys.* 305:L1

Tsuji T, Ohnaka K, Aoki W. 1999. *Ap. J.* 520:L119

Udalsky A, Szymanski M, Stanek KZ, Kaluzny J, Kubiak M, et al. 1994. *Act. Astrono.* 44:165

Ushomirsky G, Matzner CD, Brown EF, Bildsten L, Hilliard VG, Schroeder P. 1998. *Ap. J.* 253:266

VandenBerg DA, Hartwick FDA, Dawson P, Alexander DR. 1983. *Ap. J.* 266:747

White RJ, Ghez AM, Reid IN, Schultz G. 1999. *Ap. J.* 520:811

Zapatero Osorio MR, Bejar VJS, Rebolo R, Martín EL, Basri G. 1999. *Ap. J.* 524:L115
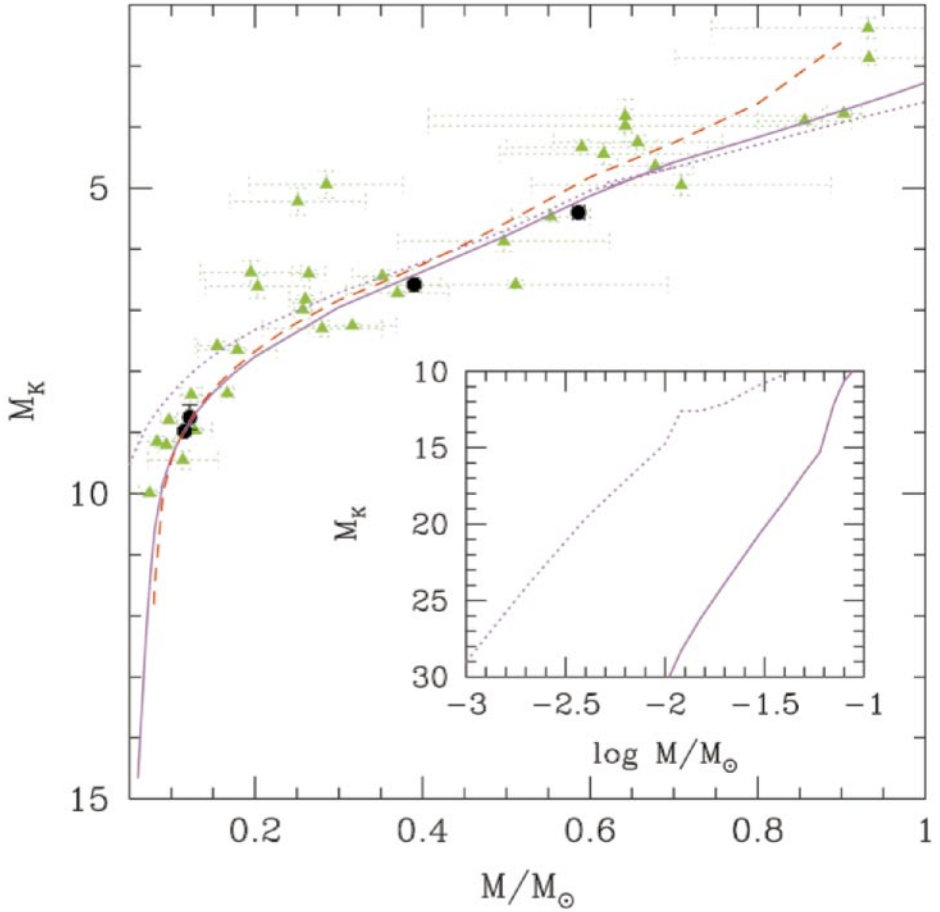
Zapolsky HS, Salpeter EE. 1969. *Ap. J.* 158: 809

Figure 9 Mass-M_K relationship. Observationally determined masses are indicated by filled triangles (Henry & McCarthy 1993) and circles (Delfosse et al 1999c, Forveille et al 1999). Solid line: $[M/H] = 0, t = 5 \times 10^9$ yr; dotted line: $[M/H] = 0, t = 10^8$ yr; dash-line: $[M/H] = -0.5$, $t = 10^{10}$ yr. NOte the log-scale in the inset.
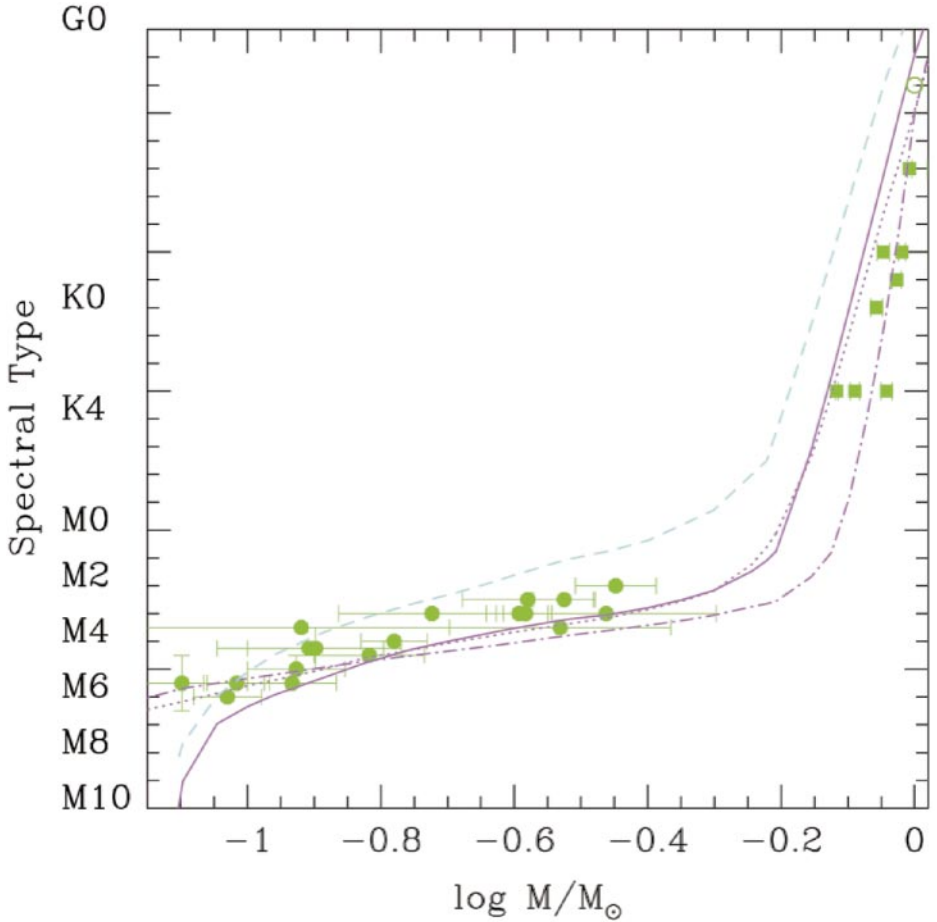
Figure 10 Mass-Spectral type relationships. Observations are from: Kirkpatrick & McCarthy (1994) for disk M-dwarfs (circles) and Clausen et al. (1999) for K- and G-dwarfs (squares). Note that the latter objects are likely to be young. The Sun is included at $S_p = $ G2. The theoretical models are from Baraffe et al (1998). Solid line: $[M/H] = 0$, $t = 5 \times 10^9$ yr; dotted line: $[M/H] = 0$, $t = 10^8$ yr; dot-dash-line: $[M/H] = 0, t = 3 \times 10^7$ yr; dash-line:$[M/H] = -0.5, t = 5 \times 10^9$ yr.
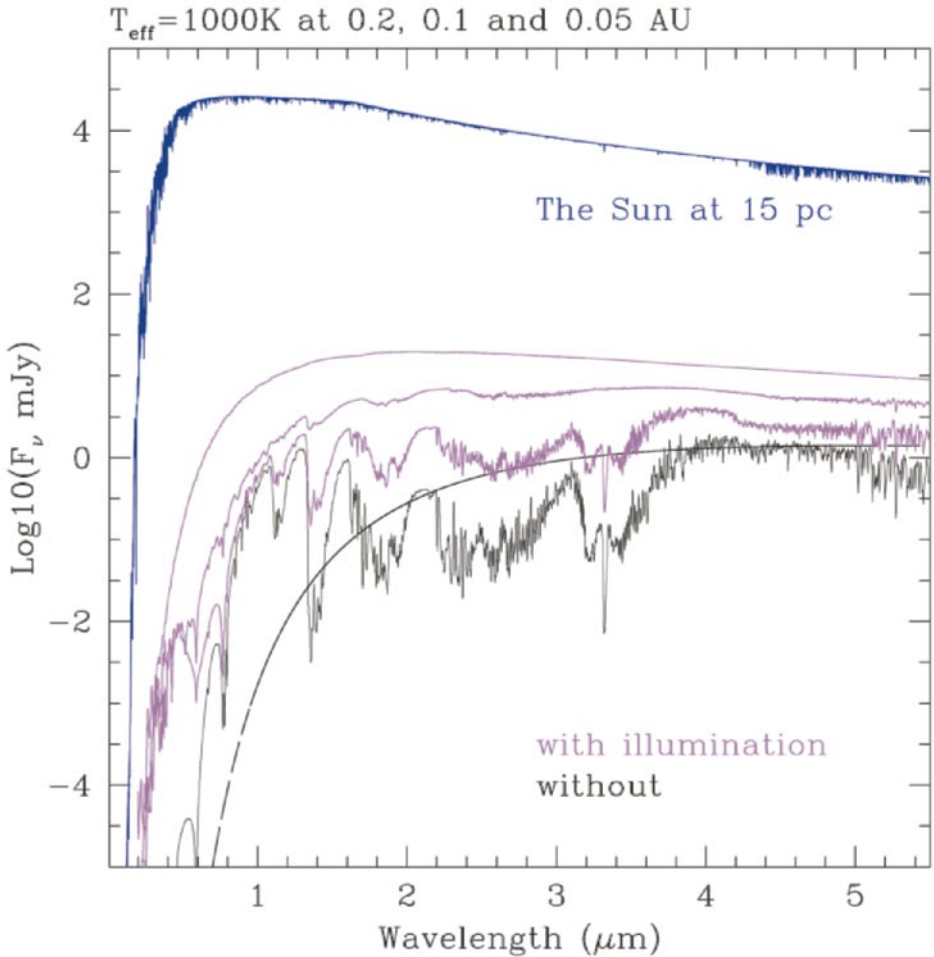
Figure 11 Spectrum of a young EGP ($T_{eff} = 1000$ K, defined as the effective temperature of the non-irradiated object) irradiated by a G2V primary at 0.2, 0.1, and 0.05 AU distance (bottom to top). The plot shows the incident spectrum (topmost curve), the spectrum emitted by the irradiated planet (magenta curves with more flux and shallower water and methane bands) and non-irradiated spectrum of the EGP (bottom full black curve) assuming a distance of 15 pc to Earth. The dashed black line is the blackbody spectrm for $T_{eff} = 1000$ K. The EGP model includes dust opacities. (Courtesy of F. Allard and P.H. Hauschildt).

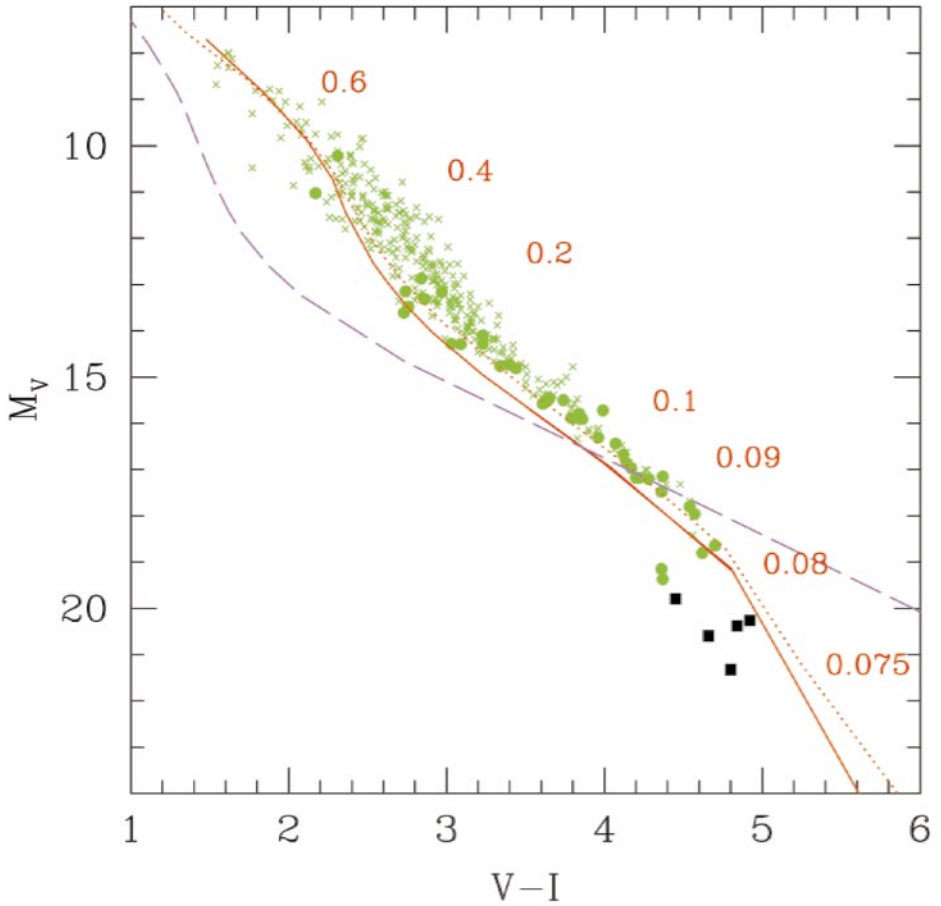**Figure 12** M_v vs (V-I) diagram for different ages and metallicites: DUSTY models (see text) for [M/H] = 0 for 10^8yr (dotted line) and 5×10^9 yr (solid line); grainless models for [M/H] = -2 and $t = 10$ Gyr (dashed line). The crosses, circles and squares correspond to observations from Dahn et al (1995), Monet et al (1992) and Dahn et al (1999), respectively. The indicated masses (in $M_\odot$) correspond to the 5 Gyr [M/H] = 0 isochrone.
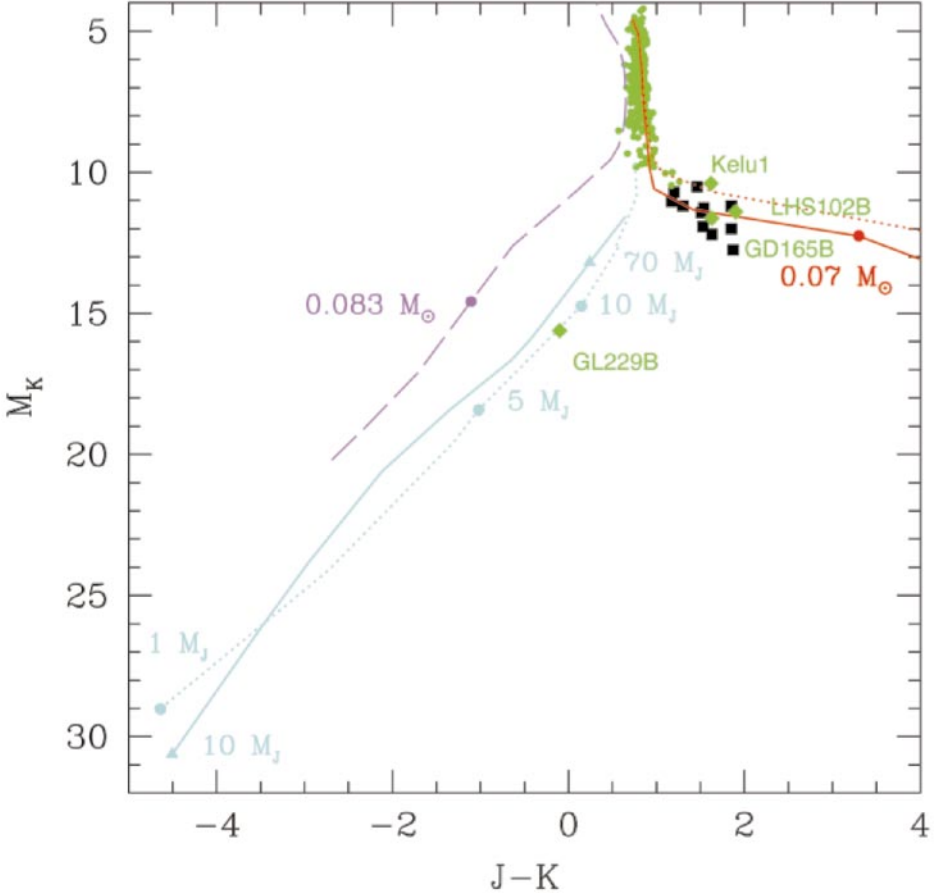
Figure 13 M_K vs (J-K) diagram for different ages and metallicites; [M/H] = 0 for 10^8 yr (dotted lines) and 5×10^9 yr (solid lines); [M/H] = −2, t = 10 Gyr (dashed line). The red curves on the right correspond to the DUSTY models for [M/H] = 0. The blue curves on the left correspond to the COND models for [M/H] = 0 (see text, §4.5.2). Filled circles and triangles on the isochrones indicate masses either in $M_\odot$ or M_J (1 $M_J \approx 10^{-3} M_\odot$). Small green circles: MS stars from Leggett (1992) and Leggett et al (1996); black squares: Dahn et al (1999). Some identified BDs are also indicated (green diamonds).
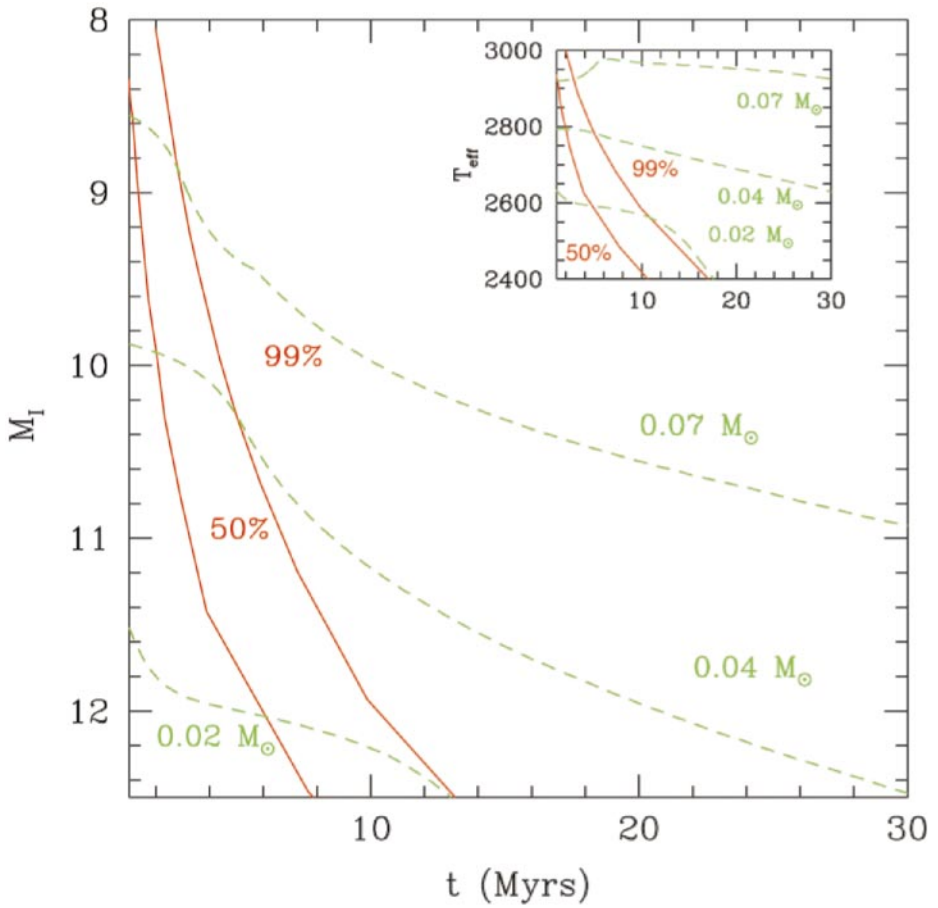
Figure 14 Deuterium-depletion curves as a function of age. The dashed lines correspond to different SSO masses, while the solid lines correspond to the 50% and 99% D-depletion limit, respectively. The inset displays the corresponding $T_{eff}(t)$.